

Design and Calibration of a Novel High Temperature Heat Flux Sensor

by
Sujay Raphael-Mabel

Thesis submitted to the Faculty of the
Virginia Polytechnic Institute and State University
in partial fulfillment of the requirements for the degree of

Master of Science
in
Mechanical Engineering

APPROVED:

Dr. Thomas E. Diller, Co-chairman

Dr. Scott Huxtable

Dr. Brian Vick

February, 2005

Blacksburg, Virginia

Keywords: Heat Flux Sensor, High Temperature, Heat Transfer

Design and Calibration of a Novel High Temperature Heat Flux Sensor

by

Sujay Raphael-Mabel

Dr. Thomas E. Diller and Dr. Scott Huxtable, Co-chairmen

Mechanical Engineering

(ABSTRACT)

Heat flux gages are important in applications where measurement of the transfer of energy is more important than measurement of the temperature itself. There is a need for a heat flux sensor that can perform reliably for long periods of time in high temperature and high heat flux environment. The primary objective is to design and build a heat flux sensor that is capable of operating for extended periods of time in a high heat flux and high temperature environment. A High Temperature Heat Flux Sensor (HTHFS) was made by connecting 10 brass and steel thermocouple junctions in a thermopile circuit. This gage does not have a separate thermal resistance layer making it easier to fabricate. The HTHFS was calibrated in a custom-made convection calibration facility using a commercial Heat Flux Microsensor (HFM) as the calibration standard.

The measured sensitivity of the HTHFS was $20.4 \pm 2.0 \mu V/(W/cm^2)$. The measured sensitivity value matched with the theoretically calculated value of $20.5 \mu V/(W/cm^2)$. The average sensitivity of the HTHFS prototype was one-fifth of the sensitivity of a commercially available HFM. Better ways of mounting the HTHFS in the calibration stand have been recommended for future tests on the HTHFS for better testing. The HTHFS has the potential to be made into a microsensor with thousands of junctions added together in a thermopile circuit. This could lead to a heat flux sensor that could generate large signals (~few mV) and also be capable of operating in high heat flux and high temperature conditions.

Acknowledgements

I would like to thank all people who played a role in my success at graduate studies and research thereby helping me develop intellectually and professionally. First, I want to express special thanks to the faculty in my research group, Dr. Thomas Diller, Dr. Scott Huxtable, and Dr. Brian Vick. I want to show my appreciation to Dr. Diller for being patient with my questions arising out of ignorance and also for helping me gain an understanding of experimentation in heat transfer research. I also want to thank Dr. Vick for helping me realize the remarkable simplicity and elegance in the concept of linearity and for making me develop a whole new way of thinking. I am deeply grateful to Dr. Huxtable for showing me support during some hard times.

I would like to show my appreciation to Dr. Mark Paul for being a great teacher and a good mentor. I also want to thank a fellow graduate student Andrew Gifford for his help in my research. My special thanks also goes to graduate students Nitin Shukla and Ashvinikumar Mudaliar for helping me brush up my long forgotten math skills and tutoring me whenever I had a hard time understanding something in fluid mechanics or heat transfer.

I also want to thank Randy Smith for putting up with me every time I pestered him to help me build my experimental apparatus and also for fixing the apparatus I managed to break. I also want to thank James Dowdy and William Songer for building all the equipment I needed for my research. A special thanks to the resident computer experts Ben Poe and James Archual for fixing all my computer problems and for being there whenever I needed them.

Finally, and most importantly, I want to thank two very special people, my parents Dr. Raphael and Mrs. Saroja Raphael for making great sacrifices to enable me pursue my dreams. I am forever in debt to them for everything they have done for me.

Table of Contents

List of Illustrations	vi
List of Tables	vi
List of Symbols	x
1.0 Introduction	1
2.0 Background	3
2.1 Need for a New Heat Flux Sensor	3
2.2 Principles of heat flux measurements	4
2.3 Type I Methods – Spatial Temperature Difference	6
2.4 Wire-Wound Gage (Schmidt-Boelter)	14
2.5 Transverse Seebeck Effect Based Sensors	16
3.0 Design and Construction of the Heat Flux Sensors	22
3.1 Fabrication of the tilted multilayer metallic structures	22
3.2 Thermopile Based Heat Flux Sensor Design	23
4.0 Test Setup and Procedure	27
4.1 Test Set Up	27
4.2 Convection Calibration Stand	27
4.3 Mounting of the HTHFS and the HFM	34
4.4 Placement of Thermocouples	37
4.5 Signal Amplifiers/Data Acquisition System and Procedure	37
5.0 Data Analysis	41
5.1 Data Reduction	41
5.2 Error Analysis	42
6.0 Results	43
6.1 Transverse Seebeck Effect Based Heat Flux Sensor	43
6.2 HTHFS with Three Brass/Steel Junctions	46
6.3 HTHFS with 10 junctions	48

6.4 Heat Transfer Coefficient	56
7.0 Discussion	60
7.1 Sensitivity of the HTHFS	60
7.2 Measured Sensitivity of the HTHFS	63
7.3 Uncertainty Analysis	65
7.4 Plot of sensitivity versus heat transfer coefficient (h)	70
7.5 Theoretical Estimation of HTHFS Sensitivity	72
8.0 Conclusions and Recommendations	74
8.1 Conclusions	74
8.2 Recommendations	75
References	76
Appendix A. HTHFS Output Plots	78
Appendix B. Experimental Determination of Seebeck Coefficient of Brass and Steel Junction	86
Appendix C. Calibration of a SB Heat Flux Gage	97
Vita	109

List of Illustrations

Fig. 2.1	Surface energy balance	5
Fig. 2.2	Example of a Type-I layered gage	7
Fig. 2.3	Thermopile circuit made of thermocouples	11
Fig. 2.4	French thin-film gage	13
Fig. 2.5	Schematic of the Schmidt-Boelter gage	15
Fig. 2.6	Anisotropic thermoelement used in the GHFS	18
Fig. 2.7	ATEs assembled in batteries	19
Fig. 2.8	Tilted metallic multi-layered structure	21
Fig. 3.1	Schematic of the thermopile circuit in the HTHFS	36
Fig. 3.2	Final prototype of the HTHFS	37
Fig. 4.1	Schematic of the test setup	29
Fig. 4.2	Convection Calibration Stand	30
Fig. 4.3	Dimensions of the tee junction	31
Fig. 4.4	Front view of the steel support frame	32
Fig. 4.5	Copper heat exchanger	33
Fig. 4.6	HTHFS attached to the surface of the aluminum plate	35
Fig. 4.7	HFM and a type – K thermocouple mounted flush with the plate surface	36
Fig. 4.8	Vatell Amplifiers	38
Fig. 6.1	Sample plot of output of TSBS for weak heated jet	44
Fig. 6.2	Sample plot of output of TSBS for strong heated jet	44
Fig. 6.3	Sample plot of output of the 3-layered TSBS for application of ice	45
Fig. 6.4	Sample plot of output of the 3-layered TSBS for strong heated jet	45
Fig. 6.5	Sample plot of output of the 3-junction HTHFS for medium heat flux	47

Fig. 6.6	Sample plot of output of the 3-junction HTHFS for strong heat flux	47
Fig. 6.7	Sample plot of HTHFS output for application of a heated weak jet	49
Fig. 6.8	Sample plot of HFM output for application of heated weak jet	49
Fig. 6.9	Sample plot of air temperature of the heated weak jet	50
Fig. 6.10	Sample HFM plate temperature for low heat flux run	50
Fig. 6.11	Sample plot of HTHFS output for medium heat flux run	51
Fig. 6.12	Sample plot of HFM heat flux data for medium heat flux run	51
Fig. 6.13	Sample plot of air temperature of the medium strength jet	52
Fig. 6.14	Sample HFM plate temperature for medium heat flux run	52
Fig. 6.15	Sample plot of HTHFS output for high heat flux run	53
Fig. 6.16	Sample plot of HFM heat flux data for high heat flux run	53
Fig. 6.17	Sample plot of air temperature of the strong jet	54
Fig. 6.18	Sample HFM plate temperature for high heat flux run	54
Fig. 6.19	Sample plot of the heat transfer coefficient of the heated weak jet	57
Fig. 6.20	Sample plot of the heat transfer coefficient of the heated medium jet	57
Fig. 6.21	Sample plot of the heat transfer coefficient of the heated strong jet	58
Fig. 7.1	Sample plot of HTHFS sensitivity for low heat flux run	61
Fig. 7.2	Sample plot of HTHFS sensitivity for medium heat flux run	61
Fig. 7.3	Sample plot of HTHFS sensitivity for high heat flux run	62
Fig. 7.4	Sensitivity of HTHFS versus heat transfer coefficient (h)	71
Fig. 7.5	Thickness 'δ' of the HTHFS	73
Fig. A.1	HTHFS output from run 1	78
Fig. A.2	HTHFS output from run 2	78
Fig. A.3	HTHFS output from run 3	79
Fig. A.4	HTHFS output from run 4	79
Fig. A.5	HTHFS output from run 5	80

Fig. A.6	HTHFS output from run 6	80
Fig. A.7	HTHFS output from run 7	81
Fig. A.8	HTHFS output from run 8	81
Fig. A.9	HTHFS output from run 9	82
Fig. A.10	HTHFS output from run 10	82
Fig. A.11	HTHFS output from run 11	83
Fig. A.12	HTHFS output from run 12	83
Fig. A.13	HTHFS output from run 13	84
Fig. A.14	HTHFS output from run 14	84
Fig. A.15	HTHFS output from run 15	85
Fig. B.1	Brass plate with type-T thermocouples	87
Fig. B.2	Brass plate in contact with melting ice	88
Fig. B.3	Voltage measurement between cold and hot junction	89
Fig. C.1	Top view of test plate	99
Fig. C.2	End view of channel and nozzle holder	100
Fig. C.3	Assembled test equipment	101
Fig. C.4	Sample heat transfer coefficient trace	104
Fig. C.5	Schmidt-Boelter sensitivity calculation	105
Fig. C.6	Air and plate temperatures	106

List of Tables

Table 7.1	Sensitivity values from each run	64
Table 7.2	Sources of uncertainty in the calibration results	67
Table 7.3	Error propagation in the sensitivity value of the HTHFS	68
Table 7.4	Sensitivity of the HTHFS and average heat transfer coefficient	69
Table B.1	Voltage between the Cu-Brass hot and cold junction	91
Table B.2	Voltage between the Constantan-Brass hot and cold junction	91
Table B.3	Voltage between the Cu-Steel hot and cold junction	92
Table B.4	Voltage between the Constantan-Steel hot and cold junction	92
Table B.5	Sensitivity coefficient of brass (Reference Material – Copper)	94
Table B.6	Sensitivity coefficient of brass (Reference Material – Constantan)	94
Table B.7	Sensitivity coefficient of steel (Reference Material – Copper)	95
Table B.8	Sensitivity coefficient of steel (Reference Material – Constantan)	95
Table C.1	Results from the calibration test	108

List of Symbols

E	Voltage output
e_x	Thermo-electromotive force
h	Convection heat transfer coefficient
k	Thermal conductivity
N	Number of thermocouple pairs
n	Number of samples
q''	Heat flux
q''_{avg}	Average heat flux
q	Heat transfer
s_m	Sample mean
S_q	Sensitivity of the gage to heat flux
S_T	Seebeck coefficient
T_1	Sensor surface temperature
T_2	Sensor surface temperature
T_g	Temperature of gage surface exposed to free stream
T_{HTHFS}	Temperature of HTHFS surface
T_{plate}	Temperature of plate surface
T_{surr}	Temperature of surrounding
T_w	Wall temperature
T_∞	Free stream temperature
α	Thermal diffusivity
δ	Thermal resistance thickness layer
μ	Sample mean

Chapter 1.0

Introduction

Heat flux gages are important in engineering applications where the measurement of the energy being transferred is more important than the temperature measurement. Such applications are found in turbomachinery research, building construction, and in industrial process control. Most heat flux gages are application specific. The gages are available commercially or custom made by the researchers. In spite of the numerous advances in the field of heat flux gage design, there still does not exist a heat flux gage that can perform for extended periods of time under high heat flux and high temperature conditions.

The newly discovered Transverse Seebeck Effect has been utilized to make heat flux gages. These heat flux gages have been made from a single crystal of bismuth and from copper-constantan multilayers. This concept had the potential to be used in a high temperature heat flux sensor. The reason is that the heat flux sensors made with the metallic multilayers had high melting points and there were no other material in the sensor. So a similar multilayered heat flux sensor was made using brass and steel layers to test the potential. The output from this sensor was not considerable and adding more layers to this sensor did not amplify the signal. Based on the results from this transverse Seebeck effect based heat flux sensor, it was decided to approach the problem in a novel manner.

The final heat flux sensor prototype given the name High Temperature Heat Flux Sensor (HTHFS) was designed by using the well known thermopile circuit in a novel manner. Previously heat flux sensors using thermopile circuits had a separate thermal resistance layer to create the thermal gradient that was measured using thermocouple junctions. The innovation in the new design is the doing away of the separate thermal resistance layer. The materials used for forming the thermocouples – in our case, brass

and steel strips – served as the thermal resistance layer. Two heat flux sensors, one with two junctions and one with ten junctions (HTHFS) were made and tested in a convection calibration facility that was designed and built specifically for the calibration of the new sensors using the HFM as the calibration standard.

The results from the test show that adding more junctions to the sensor increases the output from the heat flux sensor and the sensitivity calculated for the HTHFS matched with the theoretically calculated sensitivity. The results that were obtained from the convection calibration had some sources of error. The uncertainty in the sensitivity value due to the errors has been analyzed. The design concept for the HTHFS has been shown to work using the calibration test. Future improvements will be in the use of micro-fabrication techniques to make the HTHFS and package it to ensure proper electrical and physical isolation from its surroundings.

In summary, the following objectives were accomplished by this research: A High Temperature Heat Flux Sensor was constructed by connecting 5 brass and steel thermocouple junctions in a thermopile circuit. The novel aspect of the design was that there was no separate thermal resistance layer thus making the sensor easier to fabricate and also minimizing the thermal disruption caused by the presence of the sensor. The main objective is to show that the thermopile circuit in the HTHFS amplifies the output voltage signal as it should. A convection calibration facility was designed and built for the calibration of the HTHFS. The calibration was done using a commercial Heat Flux Microsensor and the calibration method used was the substitution method. From the calibration tests, the HTHFS was found to have a sensitivity of $20.4 \mu \text{ V}/(\text{W}/\text{cm}^2)$. This value agreed with the theoretically calculated value of $20.5 \mu \text{ V}/(\text{W}/\text{cm}^2)$. The uncertainty in the sensitivity was estimated to be about 10%.

Chapter 2.0

Background

2.1 Need for a New Heat Flux Sensor

There is a need for sensors that can measure high heat fluxes ($\sim 1 \text{ MW/m}^2$) at high surface temperatures and under large transverse gradients, for example in gas turbine research and certain industrial processes. Standard heat flux gages do not perform well under these conditions because of high temperatures and large temperature gradients. Limitation of current sensors for gas turbine applications were also discussed by Bennethum and Sherwood [1]. According to their survey, deterioration of the sensor surface due to oxidation was a problem with thin film sensors used in high temperature environments. The requirement of a cold side for the heat flux sensor installation and for routing the leads limit heat flux sensors like the embedded thermocouple gage, Gardon gage, and the slug calorimeter unsuitable for high temperature combustor component measurements.

Paulon et al. [2], Godefroy [3] also discuss techniques for high heat flux measurements in turbomachinery, particularly at high temperatures. These two researchers have fabricated thin-film heat flux sensors ($< 80 \mu\text{m}$) for use in high temperature environments. The sensors were made by forming thin film thermocouple junctions on either side of a Kapton layer. No quantitative data on the performance of the thin film sensors have been presented.

Neumann et al. [4] discuss the details of the problems in heat flux measurements encountered during hypersonic testing. Kidd [5] describes some successful heat flux measurement techniques at these high temperature, high heat flux conditions. A review of the standard methods for application to the severe conditions of the National Aerospace Plane found none of the techniques to be sufficient. Time resolved heat flux

measurements are a recent development in heat flux measurement technologies thanks to the application of thin film fabrication techniques and high speed data acquisition systems. Time resolved heat flux measurement capability and their applications were described by Diller and Telionis [6].

2.2 Principles of heat flux measurements

In areas where all three modes of heat transfer (conduction, convection, and radiation) are involved, the first law of thermodynamics is applied to the control volume containing the sensor as shown in Fig 2.1. An energy balance at the surface gives equation 2.1.

$$q_{\text{conduction}} = q_{\text{convection}} + q_{\text{radiation}} \quad (2.1)$$

The method for most heat transfer measurements is to measure $q_{\text{conduction}}$ and use equation 2.1 to infer $q_{\text{convection}}$ and/or $q_{\text{radiation}}$. The various heat flux measurement categories are given as follows:

- 1) A temperature difference is measured over a spatial distance with a known thermal resistance.
- 2) A temperature difference is measured over time with a known thermal capacitance.
- 3) A direct measurement of the energy input or output is made at steady or quasi-steady conditions. Temperature measurements are required to control or monitor conditions of the system.
- 4) A temperature gradient is measured in the fluid adjacent to the surface. Properties of the fluid are needed.

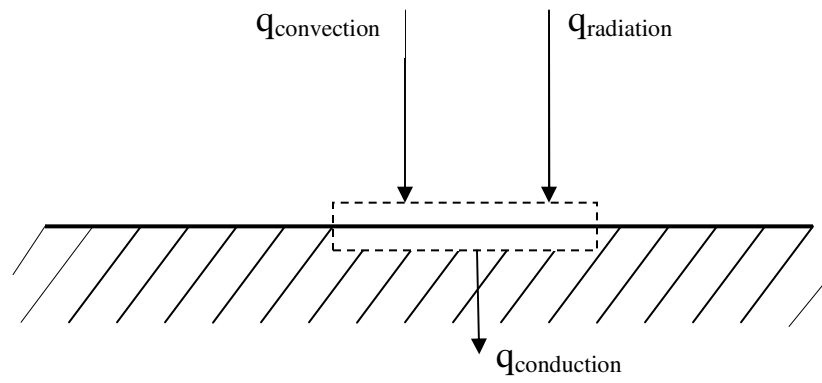


Fig. 2.1 Surface energy balance

The fourth category is not widely used and has limited applications. All heat flux gages give output signals proportional to heat flux either into or out of the surface. Heat flux gages of type I output continuous signals and as a result the heat flux through the gage can be measured as long as the signal is monitored.

2.3 Type I Methods – Spatial Temperature Difference

The simplest of type I methods is the layered gage (Fig. 2.2). The temperature is measured on either side of a thermal resistance layer and the thermal gradient is proportional to the heat flux in the direction normal to the surface. Either a Resistance Temperature Detector (RTD) or a thermocouple is used to measure the temperature. Thermocouples are usually a better choice because they can generate an output voltage without requiring external electrical excitation. Also a thermocouple is insensitive to physical strain and other factors that can affect RTD measurements.

The output of the heat flux gage is proportional to the temperature difference ($T_1 - T_2$). It can be written as

$$E = S_T (T_1 - T_2) \quad (2.2)$$

where S_T is the Seebeck coefficient of the thermocouple pair. A single thermocouple may not produce a significant amount of output voltage and hence its sensitivity may be low. The sensitivity of the gage can be improved by assembling the thermocouples in a thermopile circuit as shown in Fig. 2.3. Now, the output voltage is also proportional to the number of thermocouple pairs, N

$$E = N S_T (T_1 - T_2) \quad (2.3)$$

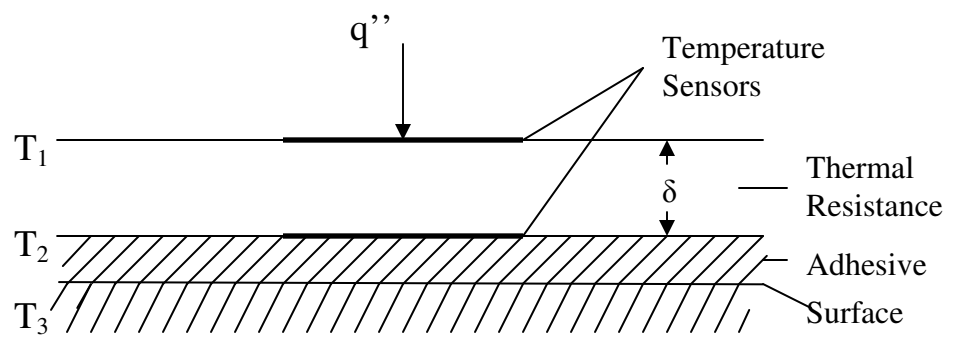


Fig. 2.2 Example of a Type-I layered gage

Thus the use of a thermopile design can significantly improve the sensitivity of the gage while maintaining the simplicity of thermocouples. Assuming one-dimensional conduction, the steady state heat conduction equation reduces to

$$q'' = \frac{k}{\delta}(T_1 - T_2) \quad (2.4)$$

So, the corresponding sensitivity of the layered gage is

$$S_q = \frac{E}{q''} = \frac{N S_T \delta}{k} \quad (2.5)$$

The transient response of the gage is a function of the thermal resistance layer thickness and the thermal diffusivity of the material. Hager [7] analyzed the one-dimensional transient response and gives the time required for 98% response as

$$t = \frac{1.5 \delta^2}{\alpha} \quad (2.6)$$

From equations 2.2 and 2.3, the sensitivity increases linearly with the thermal resistance layer thickness, but time increases as the square of the thickness. So, sensitivity versus time response is a major optimization criterion for the design of the layered gages. The errors caused by the temperature disruption of the surface are kept to a minimum if the temperature change across the gage is small, i.e.

$$\frac{T_g - T_w}{T_\infty - T_w} \ll 1 \quad (2.7)$$

where T_g is the temperature of the gage surface, T_w is the temperature of the wall on which the sensor is attached to, and T_∞ is the fluid temperature.

In the case of pure convection, this can be reduced to

$$\frac{h\delta}{k} \ll 1 \quad (2.8)$$

where h is the heat transfer coefficient.

Thermal resistance layers with thicknesses of 1 mm or more have generally been used for heat fluxes less than 1kW/m^2 . The time response is on the order of a second. For heat fluxes up to 100kW/m^2 , thermal resistance thicknesses of $25\text{-}100\ \mu\text{m}$ have been used. The corresponding time response is as low as 50 ms. The range of frequencies over which the heat flux sensor (the frequency response) can operate is low. This problem can be alleviated to some extent by using an appropriate signal conditioning circuit [6].

For low-temperature applications, Mylar or Kapton is used as the thermal resistance layer. They are versatile and easily conform to most surface shapes. The physical and thermal disruption caused by gluing the gage on to the surface during the forced convection measurements can be effectively eliminated by masking the entire surface with an equivalent thickness of the gage material. Farouk et al. [8] measured heat fluxes of $1\ \text{MW/m}^2$ in the continuous casting of metals by using chromel and alumel for the thermocouple pair with alumel for the thermal resistance layer.

Thick-film technology was used by Van Dorth [9] to put over 500 thermocouple pairs on a heat flux sensor that was 15 by 300 mm in size. This gave good sensitivity for demonstrated heat fluxes up to $200\ \text{kW/m}^2$ and temperatures up to 500°C . Hayashi et al. [10] produced thin-film heat flux gages using vacuum evaporation. A silicon monoxide layer is used instead of the adhesive layer to provide electrical insulation from the metal substrate. Two layers of nickel 0.2 mm wide and 3 mm long were deposited on either side of a second silicon monoxide thermal resistance layer. Nickel layers are used as RTDs to measure the temperature difference across the silicon monoxide layer. A bridge

circuit is used with a 1-V excitation across the two resistances to provide two output voltages, which can be linearly related to the heat flux. The gage sensitivity was found to be $S_q = 2.1 \mu\text{V/kW.m}^2$ and frequency response was estimated as 600 Hz.

An effort by French researchers to develop high-temperature heat flux gages for turbomachinery application has been reported by Godefroy et al. [11]. Their gage consists of a pair of thermocouples on either side of zirconium thermal resistance layer. Additional layers were used for physically and electrically isolating the gage from the environment and the substrate respectively. One of the layers also served as an adhesive layer. The layers were deposited by RF sputtering. No actual heat flux measurements have been published yet. The gage is shown in Fig. 2.4.

Epstein et al. [12] have produced a gage that is useful for turbomachinery research. The gage has nickel RTDs deposited on either side of a $25 \mu\text{m}$ -thick sheet of polyimide (Kapton). The sensing area is 1.0 mm by 1.2 mm. The nickel resistance element is in contact with gold leads because of the much lower electrical resistance of gold. This isolates the voltage drop of the measurement at the sensor location. The leads from the bottom element are brought through the polyimide sheet so that all four leads can be taken to the edge of the sheet together. Originally the nickel elements were vacuum deposited with dc sputtering. More recently a process of electroless plating has been used.

To avoid the physical and thermal disruption caused by placement of the gage on the measurement surface, the entire surface is completely covered with polyimide sheet to match the gage thickness. The output from the gage corresponds directly to the heat flux up to frequencies of about 20 Hz. For frequencies above 1 KHz the polyimide resistance layer appears infinitely thick and the top resistance element (T_1) responds like a Type II transient heat flux gage. To measure all frequencies from dc to 100 KHz, a numerical data reduction is used to reconstruct the heat flux signal.

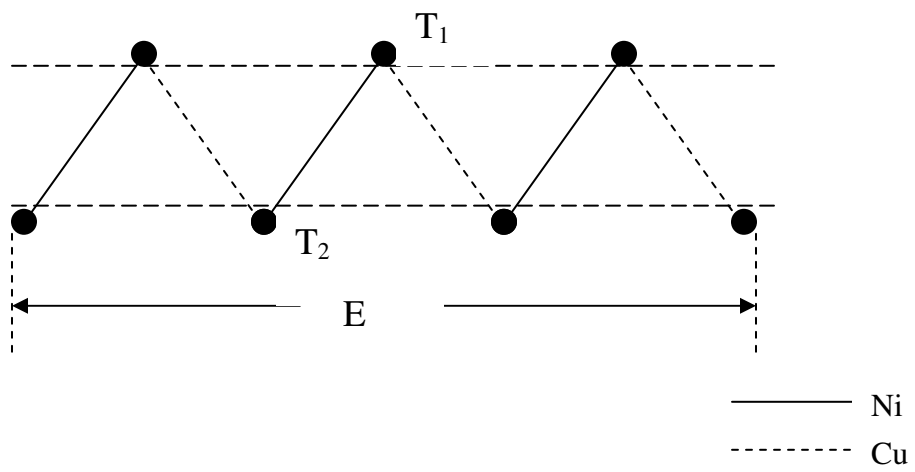


Fig. 2.3 Thermopile circuit made of thermocouples

A thinner gage by Hager et al. [13] was fabricated using thin film sputtering techniques with a thermal resistance layer of silicon monoxide that is only 1 μ m thick. The thermal disruption due to the gage is extremely small at even very high heat fluxes. The gage does not need an adhesive layer. The signal is amplified on the gage by a thermopile circuit that may consist of several hundred thermocouple pairs. The Heat Flux Microsensor is very thin (< 2 μ m) and the thermal response time is as low as 20 μ s. Use of high-temperature materials has allowed the gage to be operated at wall temperatures exceeding 1000° C.

An earlier heat flux gage that resembles the HTHFS the most was the heat flux gage designed by Farouk et al. [8] for heat flux measurements in metal castings. Their gage was made by sandwiching an alumel plate between two chromel foils. There was no separate thermal resistance layer. The sensitivity of this gage was found to be 0.66 μ V/(W/cm²).

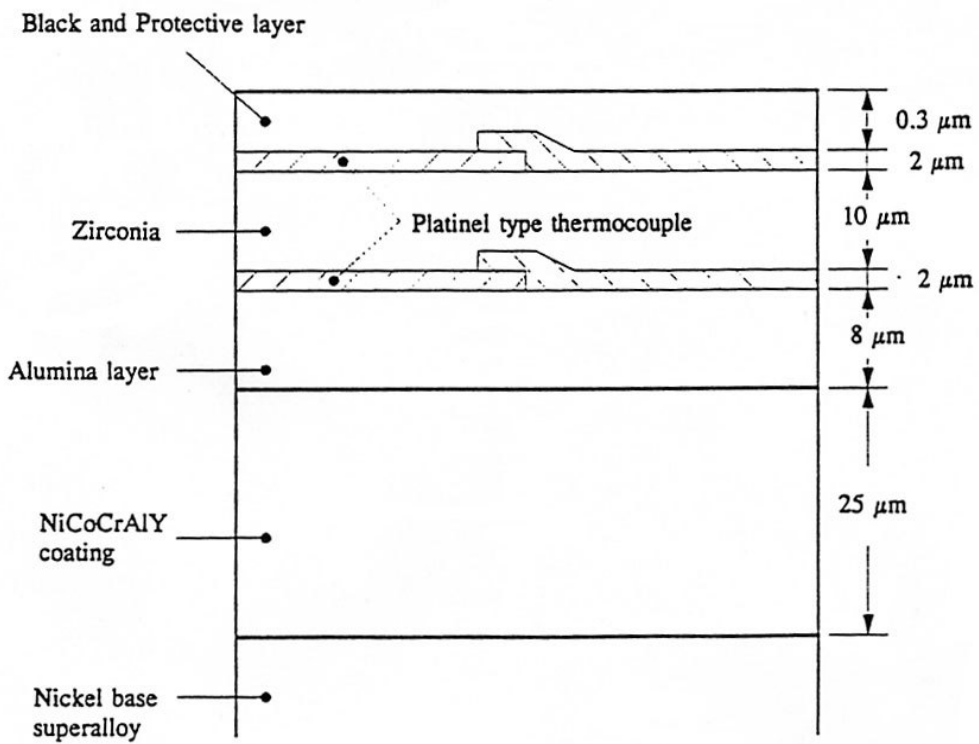


Fig. 2.4 French thin-film gage

2.4 Wire-Wound Gage (Schmidt-Boelter)

The wire-wound gage commonly known as the Schmidt-Boelter gage (Fig. 2.5) is similar to the thermopile layered gages, except for the method of fabrication of the thermocouple junctions around the thermal resistance layer. Here a fine wire of one of the thermocouple materials, usually constantan, is wrapped around the thermal resistance layer producing N number of turns. The other thermocouple material is electroplated onto one half of the wire. This forms thermocouple junctions on either side of the thermal resistance layer where the electroplating stops on the top and the bottom of the thermal resistance layer. Thus a thermopile circuit with N thermocouple junctions is formed.

The thermal resistance layer (wafer) is relatively thick (~0.5 mm) but is made of a high thermal conductivity material such as anodized aluminum. A non conductive coating on the thermal resistance layer provides electrical insulation from the bare thermocouple wires. The entire gage is placed on a heat sink and some potting material is used to smooth the sensing surface of the gage. The gage has a relatively high sensitivity and is operable in high temperatures depending upon the type of materials used for the gage.

The major drawback of this gage is that one-dimensional heat transfer is not really maintained. Significant amounts of two dimensional effects have been shown by Hayes [13] and Rougeux and Kidd [15]. Also the Schmidt-Boelter gage has been shown to lose its sensitivity to below acceptable levels for high heat flux by convection (Appendix C by Sujay and Dr. Diller).

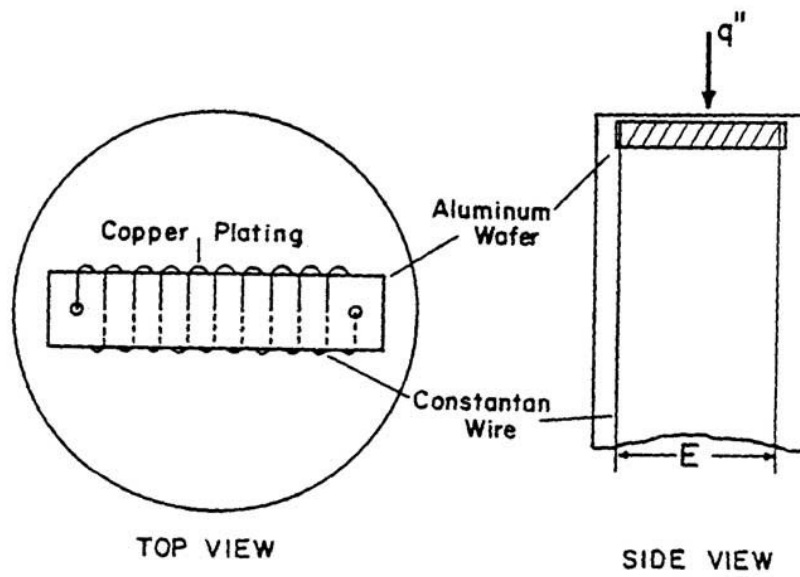


Fig. 2.5 Schematic of the Schmidt-Boelter gage

2.5 Transverse Seebeck Effect Based Sensors

A new thermoelectric effect called the transverse Seebeck effect has been observed in normal conducting, off axis grown $\text{YBa}_2\text{Cu}_3\text{O}_{7-\delta}$ (YBCO) and $\text{Bi}_2\text{Sr}_2\text{CaCu}_2\text{O}_8$ thin films. These off axis grown crystals possess anisotropic coefficients of thermoelectromotive force and thermal conductivity. Under the effect of heat flux in a direction not coinciding with the crystallographic axes of the crystal, a lateral component of electric field develops within the crystal. This thermoelectric response of the crystal is called transverse Seebeck effect. Divin [16] made the first sensor based on this principle using 0.9999 pure single crystal of bismuth.

The thermoelectric response in the crystal due to the transverse Seebeck effect is given in equation 2.9.

$$E = S \cdot \nabla T \quad (2.9)$$

where S is the Seebeck tensor and ∇T is the temperature gradient. The Seebeck tensor S is given in equation 2.10.

$$S = \begin{pmatrix} S_{11} & 0 & S_{13} \\ 0 & S_{ab} & 0 \\ S_{11} & 0 & S_{33} \end{pmatrix} \quad (2.10)$$

For a rectangular coordinate system and with the crystal 'c-axis' oriented at an angle α to the horizontal, the components of the tensor are given in equations 2.11, 2.12, and 2.13.

$$S_{11} = S_{ab} \cos^2 \alpha + S_c \sin^2 \alpha \quad (2.11)$$

$$S_{33} = S_{ab} \sin^2 \alpha + S_c \cos^2 \alpha \quad (2.12)$$

$$S_{13} = S_{31} = \frac{1}{2}(\sin 2\alpha)(S_{ab} - S_c) = \sin \alpha \cos \alpha . \Delta S \quad (2.13)$$

where S_c and S_{ab} are the values of the thermoelectric power along the crystal ‘c-axis’ and within the ‘ab-plane’ respectively [17].

A Gradient Heat Flux Sensor (GHFS) using an anisotropic thermoelement cut from a single crystal of bismuth was built and tested by Mityakov et al. [18]. A schematic of the anisotropic thermoelement (ATE) is shown in Fig. 2.6. The heat flux is in the direction of the z-axis and the transverse Seebeck effect acts in the x-direction causing a thermoelectric force to emerge in the x-direction.

The thermoelectric force is proportional to the heat flux density as predicted by Fourier’s law and is given by equation 2.14.

$$e_x = \frac{(\varepsilon_{33} - \varepsilon_{11}) \sin \theta \cos \theta}{\sqrt{\lambda_{33}^2 \sin^2 \theta + \lambda_{11}^2 \cos^2 \theta}} F q_z \quad (2.14)$$

Here ε_{11} and ε_{33} are components of the tensor of differential-thermoelectric force, λ_{11} and λ_{33} are the components of the thermal conductivity tensor, $F = 1 \times b$ is the area of the ATE in plan, and q_z is average density of the external heat flux. The sensitivity of the single element sensor is given in equation 2.15.

$$S_q = \frac{e_x}{q_x F} \left(\frac{V}{W} \right) \quad (2.15)$$

Since the output voltage from a single sensor element is considerably small, the ATEs are assembled in batteries (Fig. 2.7). The batteries are assembled in such a way that the thermoelectric force arising from each trigonal summed up. The Gradient Heat Flux Sensor was calibrated by the absolute method (Joule-Lenz heat flux).

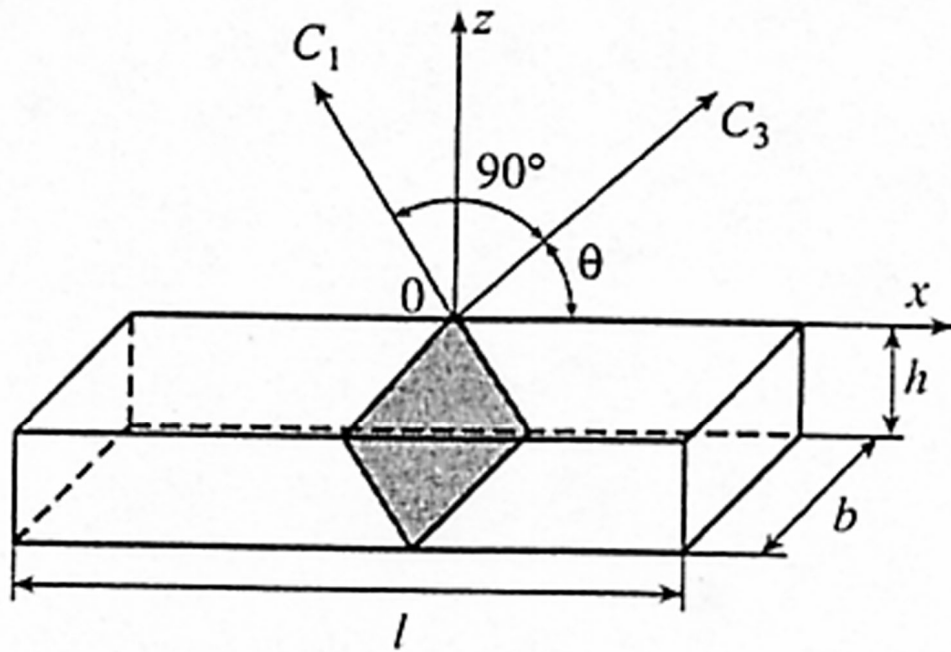


Fig. 2.6 Anisotropic thermoelement used in the GHFS

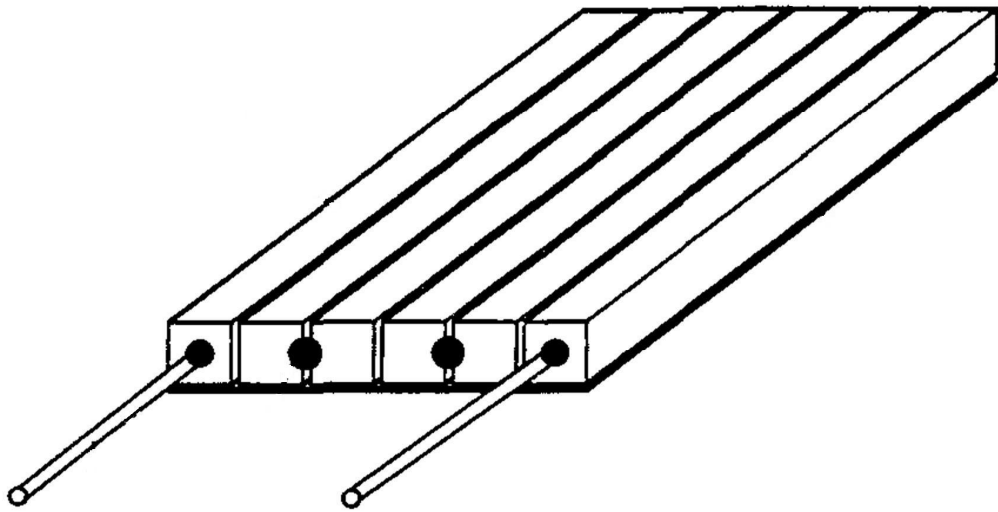


Fig. 2.7 ATEs assembled in batteries

The sensor was able to operate in a maximum heat flux density of 1 MW/m^2 . Dynamic tests of the GHFS were done using a pulsed thermal laser. The authors claim that the GHFS has a time constant on the order of $50 \text{ }\mu\text{s}$ but the sources of this result are not verifiable.

Zahner et al. [19] fabricated a transverse Seebeck effect based heat flux sensor using copper and constantan multilayers. Here the thermal anisotropy was created by a tilted metallic multilayer structure (Fig. 2.8) was prepared by sintering a compressed stack of copper/constantan foils, each with a thickness of 0.1 mm . The test samples were obtained by cutting the sintered stack obliquely to its axis. Samples with varying tilt angles α were made with sample thickness of $\sim 1 \text{ mm}$.

A sample with a length of 8 mm between contacts, width 6 mm , thickness 2 mm , and tilt angle $\alpha = 15^\circ$ was heated with a diode laser irradiation ($\lambda = 689 \text{ nm}$, $P = 10 \text{ MW}$) of the sample surface. The sample surface was blackened to improve absorption. For pulse duration of 0.1 s , an output of 150 nV was measured. On further testing samples with different tilt angles α with a constant irradiation of 10 MW/cm^2 , the maximum output occurs at a tilt angle of 25° .

A sensor with a tilt angle $\alpha = 35^\circ$ and a thickness of $10 \text{ }\mu\text{m}$ was irradiated with a pulse of Nd:YAG laser ($\lambda = 1064 \text{ nm}$, pulse duration $\sim 15 \text{ ns}$, $E_{\text{pulse}} = 0.5 \text{ mJ/cm}^2$). The recorded signal height was 1 mV and the decay was within several μs . Thus it was found that artificially created tilted metallic multilayer structures exhibit transverse Seebeck effect similar to $\text{YBa}_2\text{Cu}_3\text{O}_{7-\delta}$ and $\text{Bi}_2\text{Sr}_2\text{CaCu}_2\text{O}_8$ superconductor films in the normal state.

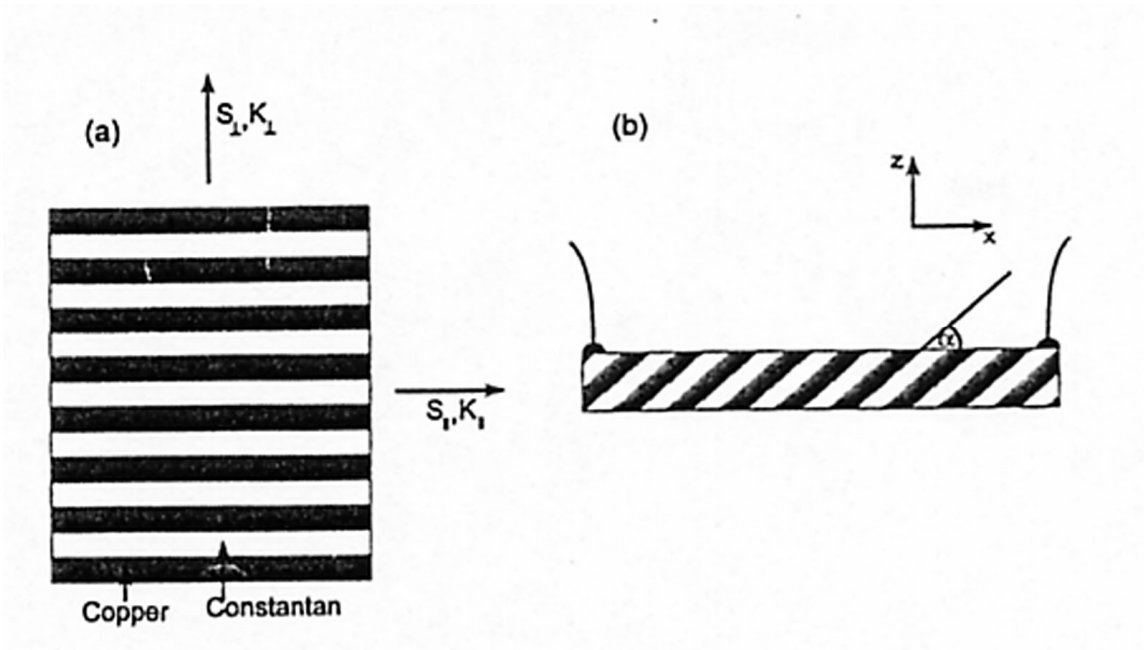


Fig. 2.8 Tilted metallic multi-layered structure

Chapter 3.0

Design and Construction of the Heat Flux Sensors

All sensors previously reviewed are not operable in high temperature conditions for extended periods of time. Most of the high sensitivity heat flux sensors like Vatel Corporation's HFM used a thermopile circuit with thermocouple junctions formed on either side of a thermal resistance layer. The presence of the thermal resistance layer increases the sensitivity but also increases the time constant of the response signal. The transverse Seebeck effect based Gradient Heat Flux Sensor and the sensor by Zahner et al. [17] did not use a thermal resistance layer. Rather the thermo-electromotive force was generated by the anisotropic Seebeck coefficients and thermal conductivities caused by tilted crystal structures or multiple metallic layers.

Since the transverse Seebeck effect based sensors gave large outputs (~1 mV), the first approach was to build a sensor similar to these sensors to verify if such large outputs are possible. The GHFS was not attempted because the single crystal bismuth used to make the sensor melts at around 250° C. The tilted multilayered metallic sensor by Zahner et al. [17] was a better choice because they used metals that have better survivability in high temperatures. So, an artificially tilted multilayered metallic sensor was made using steel and brass layers. The reason for choosing steel and brass was the ease of their availability. Other combinations of common thermocouple materials like nickel, copper, and platinum may be used in future designs.

3.1 Fabrication of the tilted multilayer metallic structures

The tilted multi-layered metallic structures with copper and constantan layers by Zahner et al. [19] were created by sintering of copper and constantan foils kept in compression. The underlying requirement for this structure to work well is good electrical contact between two adjacent layers. Realizing this fact, each layer of brass

and steel were individually machined. Twenty three pieces (elements) each were made from each material (brass and steel). Each element was tilted at an angle of 45° .

A box was made from Lexan plastic to hold the sensor elements together such that it formed the tilted multilayered metallic structure. The slot on the top surface of the box was made with a 45° tilt at the opposing edges to accommodate the 45° tilt of the sensor elements. The brass and the steel elements were inserted lengthwise into the slot alternatively until all the 46 elements were inserted into the slot. The elements were placed snug in the slot such that all of the sensor elements were in good electrical and thermal contact with each other. The outer layers in the sensor were brass elements. A brass wire was soldered onto the outer brass elements to measure the thermoelectromotive force that is developed in the transverse direction of the sensor in response to a heat flux applied normal to the surface.

Heat flux tests done on this sensor showed that the output was low ($\sim 5 \mu\text{V}$) for heat flux of roughly 1.5 W/cm^2 (this number is only an estimate using data from later experiments as the actual heat flux was not calculated at this time). Increasing or decreasing the number of layers did not bring about considerable change. The sensitivity shown by this sensor was not considered acceptable. Therefore, a different approach was tried using the same sensor elements. That design is described next.

3.2 Thermopile Based Heat Flux Sensor Design

Following the mediocre output from the transverse Seebeck effect based sensor, that idea was abandoned. Instead the following changes were made in the sensor design. Eleven elements (steel-5, brass-6) were made to the following dimensions (1.7 cm x 0.5 cm x 0.1 cm) and there was no tilt angle incorporated into the layers.

A new sensor holder was made for the new sensor. The sensor holder was open on both sides so that the sensor elements can be made to come into thermal contact with a metal substrate unlike the earlier box where the bottom side of the sensor was closed by

the box. In the earlier box, the heat flux had no place to go once it reached the bottom end of the sensor and so a steady heat transfer rate could not be reached.

The sensor elements were put together in a thermopile circuit using the following procedures. A junction was formed between two adjacent sensor elements by soldering them together at one of the tips. The rest of the space between the two elements is electrically isolated by using an insulator between the two elements. Junctions like this were made on the top and the bottom alternatively such that the junctions added up in a series circuit as shown in the Fig. 3.1. The final prototype of the HTHFS is shown in Fig. 3.2. Each of the junctions was a thermocouple and the Seebeck coefficient of the brass/steel combination was determined (Appendix B).

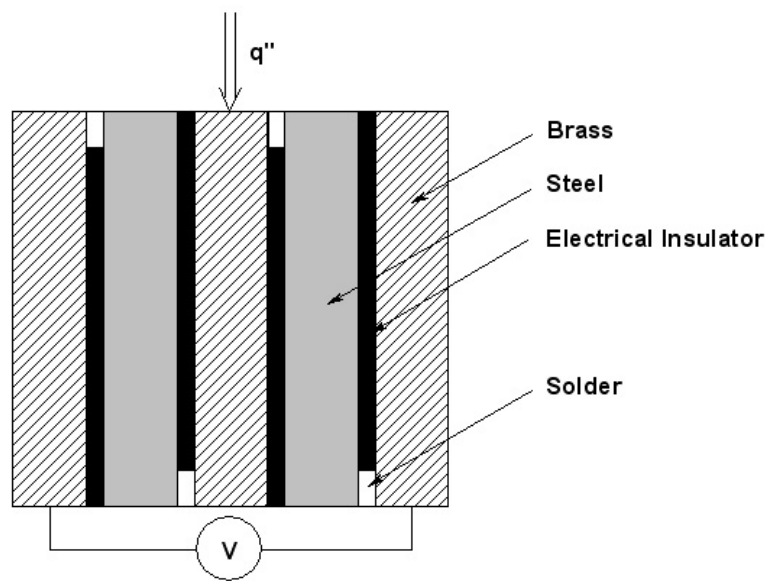


Fig. 3.1 Schematic of the thermopile circuit in the HTHFS

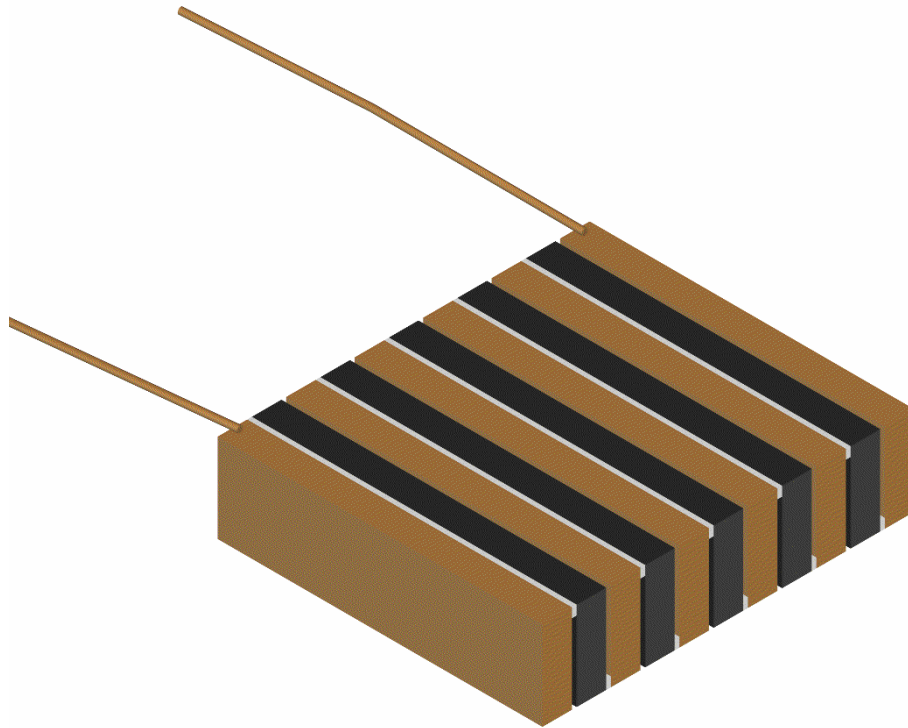


Fig. 3.2 Final prototype of the HTHFS

Chapter 4.0

Test Setup and Procedure

In this chapter, a description of the test facility, the equipment used for the experiments, and the procedures for the experiment is given. The chapter is divided into brief sections describing the overall test setup, the test rig used for calibrating the heat flux gage, the test gage, the HFM heat flux gage, the amplifiers for the HFM gage and the test heat flux gage, the data acquisition system, and the experimental procedure.

4.1 Test Setup

The setup for this experiment was created in the Supersonic Wind Tunnel Laboratory at Virginia Polytechnic Institute and State University. The complete test setup consists of a pressure vessel, tubing to carry the air supply, a copper coiled tube that functioned as a heat exchanger to heat or cool the air, and a convection calibration stand. A schematic of the entire test setup is shown in Fig. 4.1.

4.2 Convection Calibration Stand

The Convection Calibration Stand (Fig. 4.2) was built in such a way as to measure the output of the test heat flux gage while simultaneously measuring the output from a known HFS gage. The Convection Calibration Stand used for testing and calibration of the sensor consists of a tee junction attached to a steel support frame. The support frame also holds two aluminum plates one of which holds the test sensor and the other the reference HFS gage.

The support frame and the tee junction are made of stainless steel and the channels that support the sensor mounting plates are made of aluminum. Air is supplied to the nozzle from a large pressure vessel that is pressurized to about 120 psi using ½” inner diameter plastic tubes. The air is heated or cooled before it enters the tee junction using a copper heat exchanger.

The leg of the tee junction (Fig. 4.3) has an inner diameter of 3/8" and it splits into two 1/4" inner diameter nozzles. The diameter of the nozzles was made smaller than the diameter of the supply pipes so that when choked flow occurs, the choking takes place at the nozzles.

The steel support frame (Fig. 4.4) is constructed such that it resembles a bridge. The tee junction is attached through an orifice in the support frame. The other side of the frame is fitted with an adapter to attach to a 1/2" inner diameter tube. Four aluminum channels are placed at each inner and bottom corner of the support. The purpose of these channels is to hold two aluminum plates such that the air jets from the nozzles impinge on their faces perpendicularly. The spacing between the nozzle exit and the face of the aluminum plates was calculated as approximately 7 times the nozzle exit diameter. This spacing was chosen so as to maximize the heat flux on the sensors.

The copper heat exchanger (Fig. 4.5) consists of a coiled copper tube made of soft copper tube (1/2" I.D.). The coil has an outer diameter of 8.5" and has 7 turns. The heat exchanger is heated or cooled by immersing it in boiling water or melting ice. Air supply into and out of the heat exchanger is carried by insulated plastic tubes (1/2" I.D.)

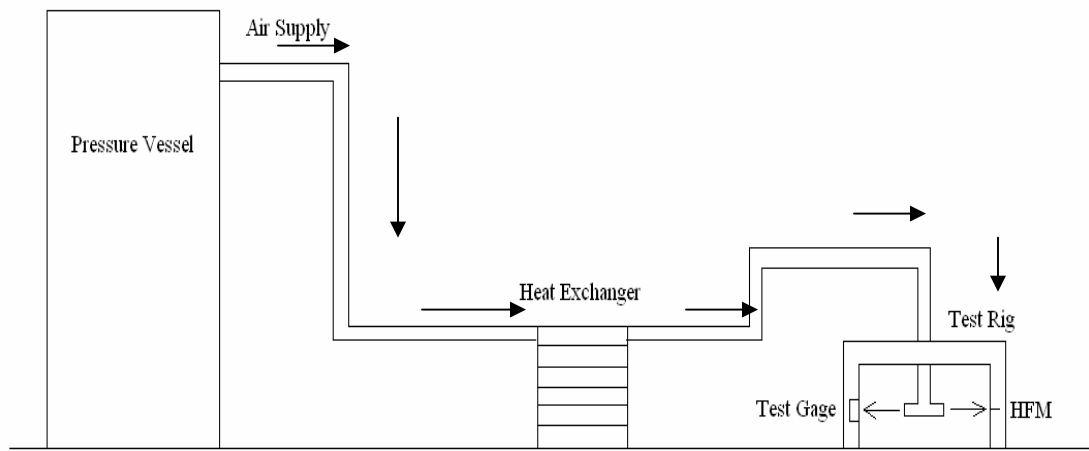


Fig. 4.1 Schematic of the test setup

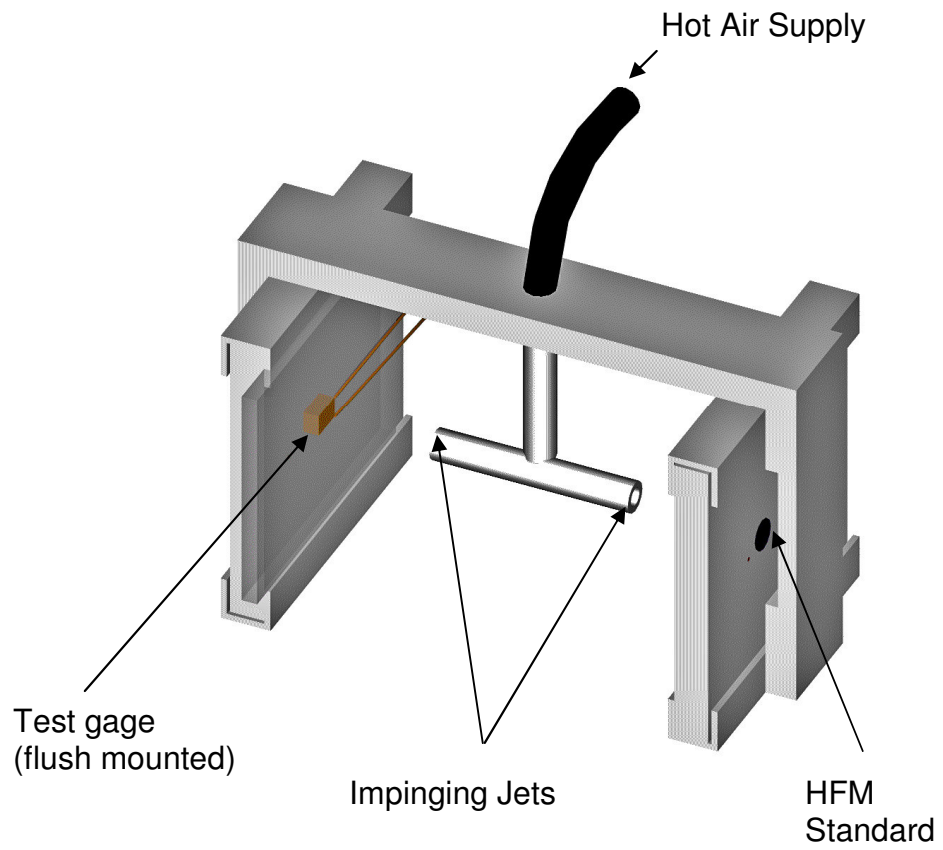


Fig. 4.2 Convection Calibration Stand

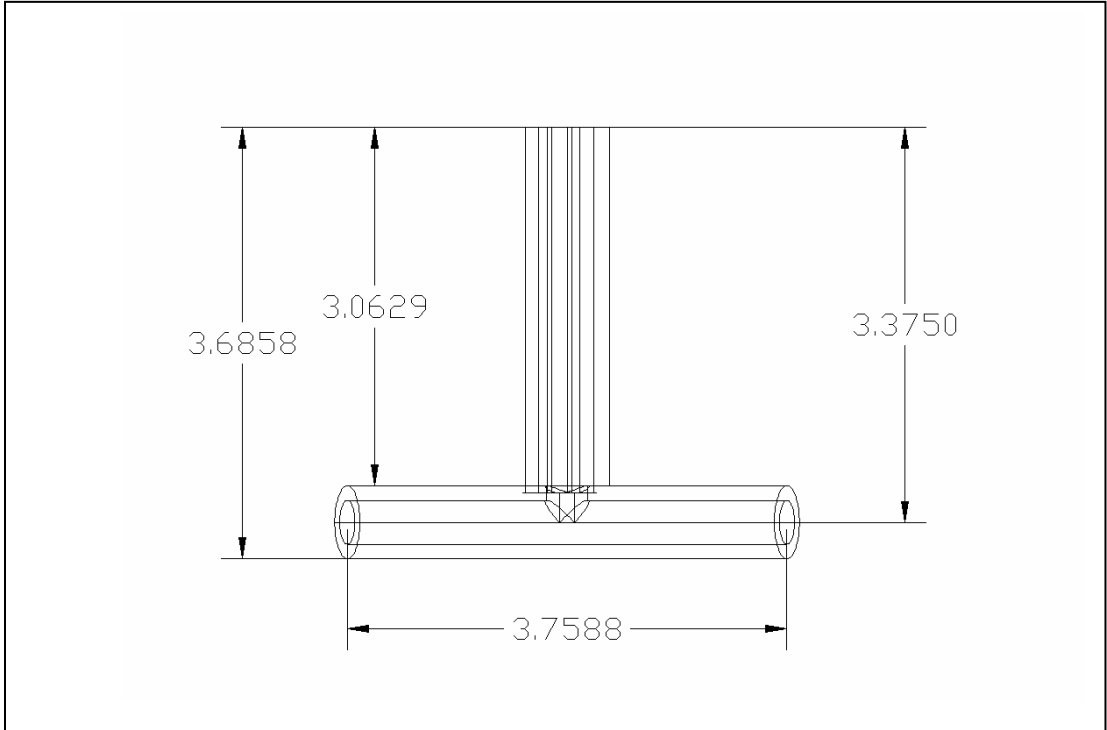


Fig. 4.3 Dimensions of the tee junction

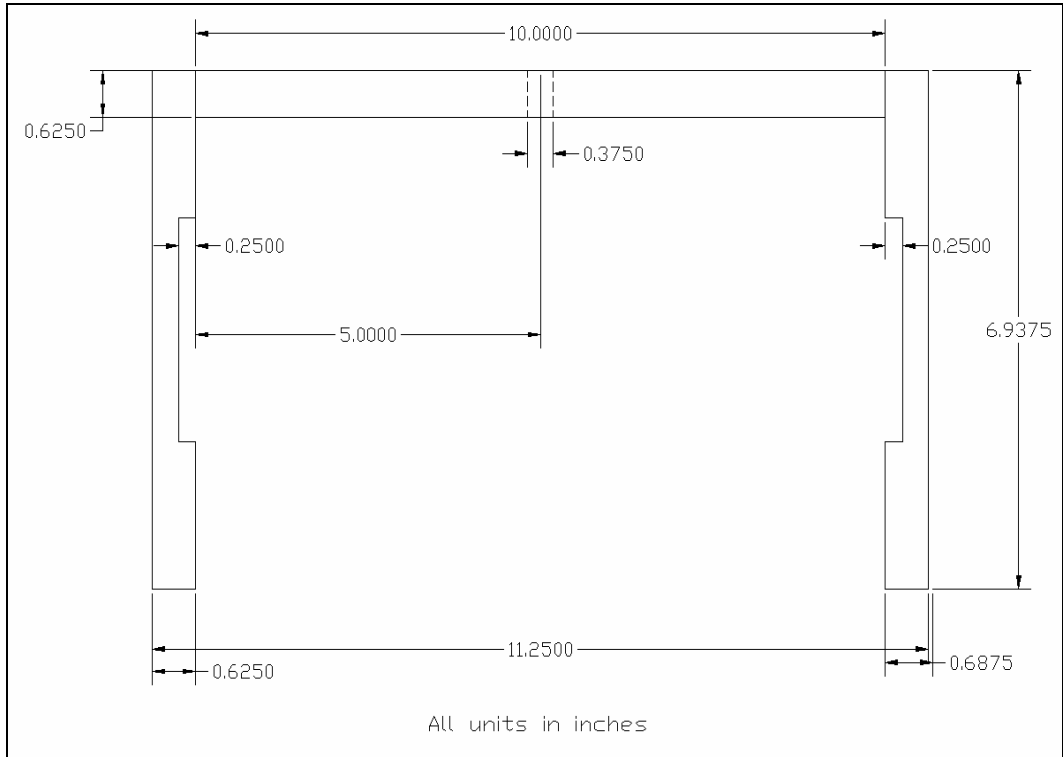


Fig. 4.4 Front view of the steel support frame



Fig. 4.5 Copper heat exchanger

4.3 Mounting of the HTHFS and the HFM

The test gage was flush mounted on the surface of the plate using a Lexan plastic holder. A thin plastic film was placed between the gage and the aluminum plate to prevent electrical contact between the plate and the test gage. A thin layer of thermal paste was applied between the test gage and the plastic film to ensure proper thermal contact between the test gage and the plate surface. The HTHFS mounted flush with the Lexan holder is shown in Fig. 4.6. The HFM gage was mounted through a hole flush with the surface of the plate (Fig. 4.7).

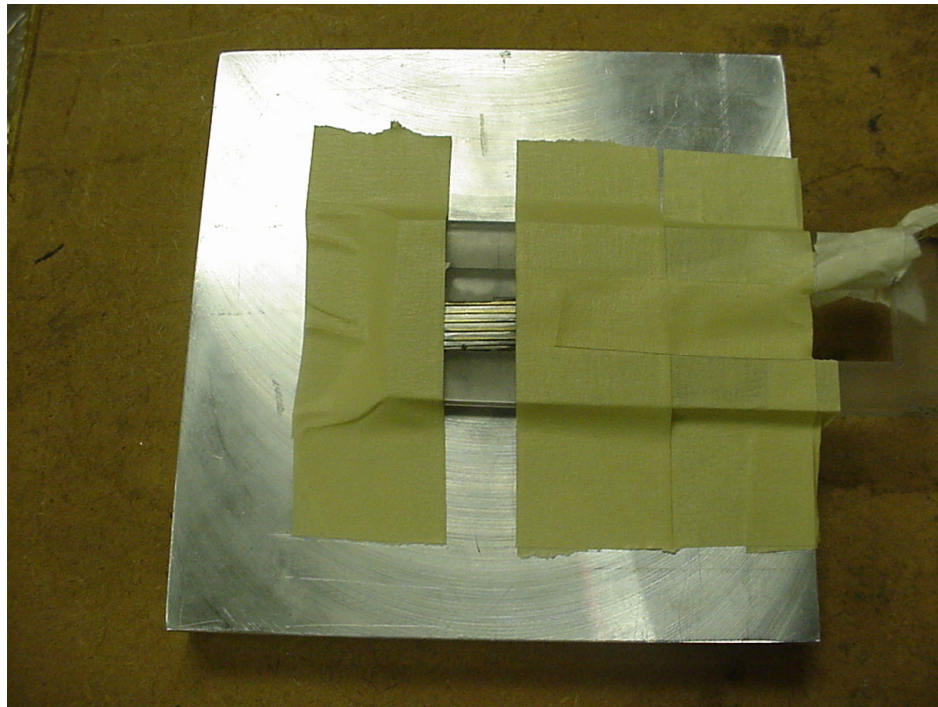


Fig. 4.6 HTHFS attached to the surface of the aluminum plate

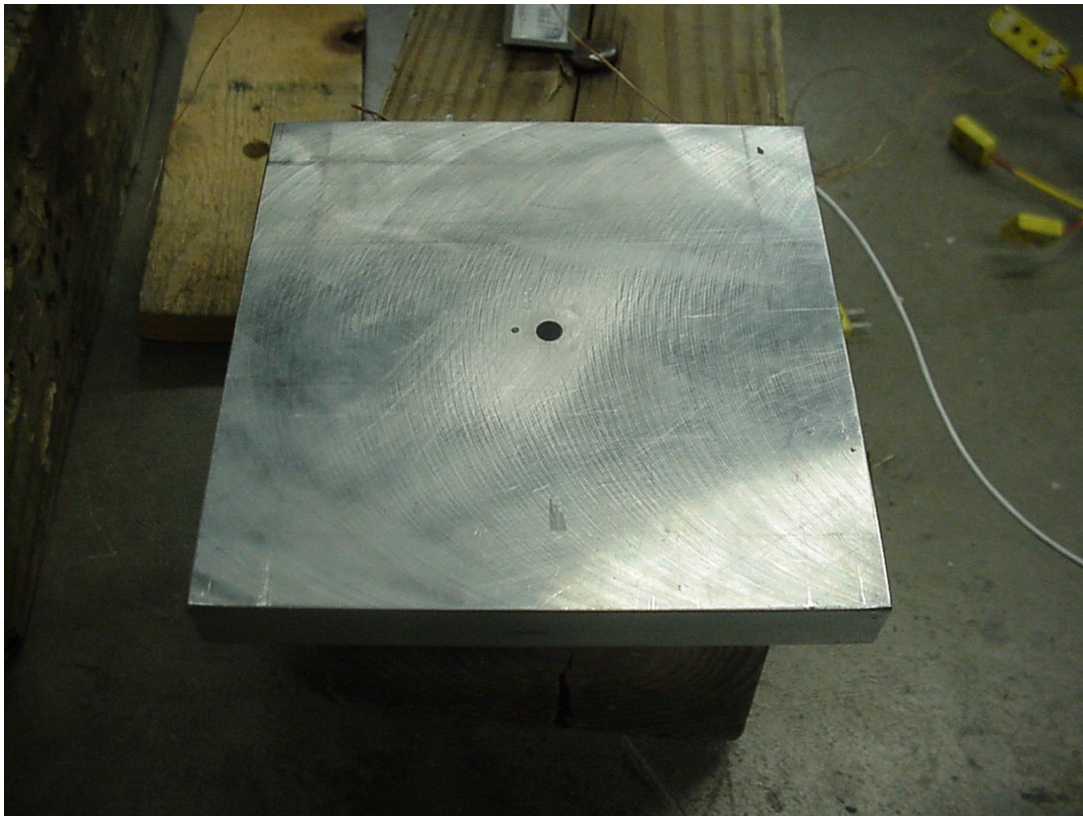


Fig. 4.7 HFM and a type – K thermocouple mounted flush with the plate surface

4.4 Placement of Thermocouples

Two thermocouples were inserted into the Convection Calibration Stand to measure the temperature of the air jet and the temperature of the plate surface in which the HFM is flush mounted. For measuring the temperature of the plate surface, a type K thermocouple was mounted through a hole flush with the surface. The thermocouple was placed close to the HFS gage. The thermocouple was flush mounted by the following procedure: A 1/16" diameter hole was drilled in the desired location on the plate. The type K thermocouple was inserted through the hole and then through 1/16" diameter copper tube. The thermocouple junction was soldered on to the end of the copper tube. The copper tube along with the thermocouple is flush mounted by press fitting it into the 1/16" diameter hole.

4.5 Signal Amplifiers/Data Acquisition System and Procedure

The voltage signal from the HFM was amplified by a signal amplifier designed specifically for the HFM by Vatec Corporation (Fig. 4.8). Both amplifiers were set at a gain of 100 and were zeroed so that zero heat flux corresponded to zero output. The signals were fed into an IBM PC through a data acquisition card and the data was acquired and recorded in ASCII text format using LabVIEW. The data was later imported into Microsoft Excel in spreadsheet format and analyzed.

The experiment for testing and calibrating the test gage was conducted in such a way as to measure the response of the test gage to varying levels of heat flux: strong, medium, and weak jets. The reference HFM gage with a known sensitivity is also applied with the same heat flux that is incident on the test gage and using the signal from the HFM heat flux gage, the sensitivity of the test gage is calculated. The detailed procedures involved in each run are given in the following.



Fig. 4.8 Vatec Amplifiers

The pressure vessel was pressurized to a pressure of between 120 and 160 psi using a compressor. At these pressures, the pressure vessel was capable of delivering strong jets for the period of the entire experiment. The outlet from the pressure vessel is connected to the heat exchanger and the outlet from the heat exchanger is connected to the inlet of the tee junction in the Convection Calibration Stand. When the pressure vessel was being pressurized, a pot of water was heated on a hot plate to boil. The copper coiled heat exchanger was immersed in the boiling pot of water. The air was heated when it flowed through the heat exchanger.

Before the tests were run, the test gage and the HFM heat flux gage was connected to the appropriate amplifiers. The amplifier gains were set at 100. The outputs from the two amplifiers and the two type-K thermocouples were connected to the data acquisition board, which in turn was connected to the computer. The signal from the data acquisition board was recorded by LabVIEW. The LabVIEW program was customized for the calibration experiments. The sampling frequency was set at 100 Hz and the sampling time was 10 to 15 seconds. The sampling rate was chosen to capture the time varying component of the heat flux measurement if any. The sampling time was chosen for the convenience of the experimenter.

The LabVIEW program captured four signals: the test gage output, the HFM output, and two type-K thermocouple signals. The signals from the test gage and the HFM were in voltages and were resolved to ± 0.1 mV and the signals from the type-K thermocouples were directly converted to temperature readings in degrees Celsius using an internal reference. The thermocouple signals were resolved to $\pm 0.1^\circ\text{C}$. The signals from the test gage and the HFM represented the magnitude of the heat flux being applied by the heated or cooled jet. The thermocouple embedded in the tee junction measured the temperature of the heated jet and the thermocouple embedded near the HFM measured the temperature of the plate.

The strength of the air jet can be controlled by a valve on the pressure vessel. The test runs started with a weak jet and then later the strength was increased to a medium jet and finally to a strong jet. Once the strength of the air flow is established at the required level, the outlet valve is completely turned on. The test gage and the HFM were blocked from the impinging air jets by using blocks of wood. The air jet was allowed to run for a few minutes until the air supply from the jet was sufficiently heated. This time delay was caused because the air had to heat the supply tube. Once a steady-state temperature was reached, the LabVIEW data acquisition was turned on from the PC and the blockages between the air jets and the sensors were removed. When the data acquisition was over, the air jet was turned off. The acquired data was stored in ASCII text files, which were analyzed later using MS-Excel.

Chapter 5.0

Data Analysis

5.1 Data Reduction

After the calibration tests were run, the voltage signal from the High Temperature Heat Flux Sensor (HTHFS), the HFM, the temperature of the air in the tee junction, and the temperature of the HFM mounted plate were acquired. The data from the calibration runs were used to determine the sensitivity of the HTHFS. The output from the HFM was used to determine the average heat transfer coefficient 'h' during each run.

The process of reducing the data started with plotting the four signals against time. The heat flux was started a few minutes after data acquisition began. So, there is a zero offset voltage in the signals from the two sensors before the actual output starts. The average value of the zero offset voltage in the HTHFS signal and the average value of the zero offset voltage in the HFM signal were computed using Excel. Similarly, the average value in the output voltage of the HTHFS and the HFM were computed using Excel. The average heat flux during each run was calculated using equation 5.1.

$$q''_{avg} = \frac{\text{Average HFM output (Volt)} - \text{Average HFM offset voltage}}{\text{Gain} \times \text{Sensitivity of the HFM} \left(\frac{\text{Volt}}{\text{W / cm}^2} \right)} \quad (5.1)$$

The gain for both amplifiers was set at 100 and the sensitivity of the HFM is $100 \mu \text{V}/(\text{W}/\text{cm}^2)$. After the average heat flux value had been determined, the sensitivity of the HTHFS was calculated using Equation 5.2

$$S_q = \frac{\text{Average HTHFS output (Volt)} - \text{Average HTHFS offset voltage}}{\text{Gain} \times q''_{avg}} \quad (5.2)$$

A heat transfer coefficient for the jet was calculated at each time instant using the equation 5.3:

$$h = \frac{q''_{avg}}{T_{\infty} - T_{plate}} \quad (5.3)$$

5.2 Error Analysis

The uncertainty in the results obtained for the sensitivity of the HTHFS and the heat transfer coefficient (h) was estimated by using statistical analysis (Type A method). Also the manufacturer's specifications for the HFM and the amplifiers were used to determine the uncertainty caused by the equipment. The random error in the distribution of the sensitivity of the HTHFS and the heat transfer coefficient was estimated by approximating the distributions as a Student's t-distribution and a normal distribution respectively. The heat transfer coefficient can be approximated by a normal distribution because the number of samples is large (~1000 samples). The uncertainty in a quantity caused by the random error was estimated as the standard deviation in the distribution of the mean of the quantity for a 95 % confidence interval. All statistical analyses were done using MS-Excel's Analysis Toolpak.

Chapter 6.0

Results

This chapter presents the results obtained from the calibration tests done on the HTHFS. The results from testing a sensor that was based on the transverse Seebeck effect and a three junction HTHFS are also presented here. A discussion of the results is presented in each of the individual sections and chapter 7.

6.1 Transverse Seebeck Effect Based Heat Flux Sensor

The prototype Transverse Seebeck Effect based Sensor (TSBS) made up of 46 layers of steel and brass was tested with a heated jet and with manual application of ice. From Fig. 6.1 and 6.2, it can be seen that the heat flux sensor is responding to increases in the amounts of heat flux, although the difference in output between the low heat flux test and the high heat flux test was not much. The distinct peaks seen at regular intervals in the signal plots may be electrical noise that may have been picked up by the exposed wires connected to the HTHFS.

An experiment was made to determine if there is any change in the signal magnitude for change in the number of tilted metallic layers. So, instead of 46 layers of metal, a sensor made of three layers – two brass layers on the ends and a steel layer in the middle – was built. The heat flux tests on this sensor gave the output that is plotted in Fig. 6.3 and 6.4.

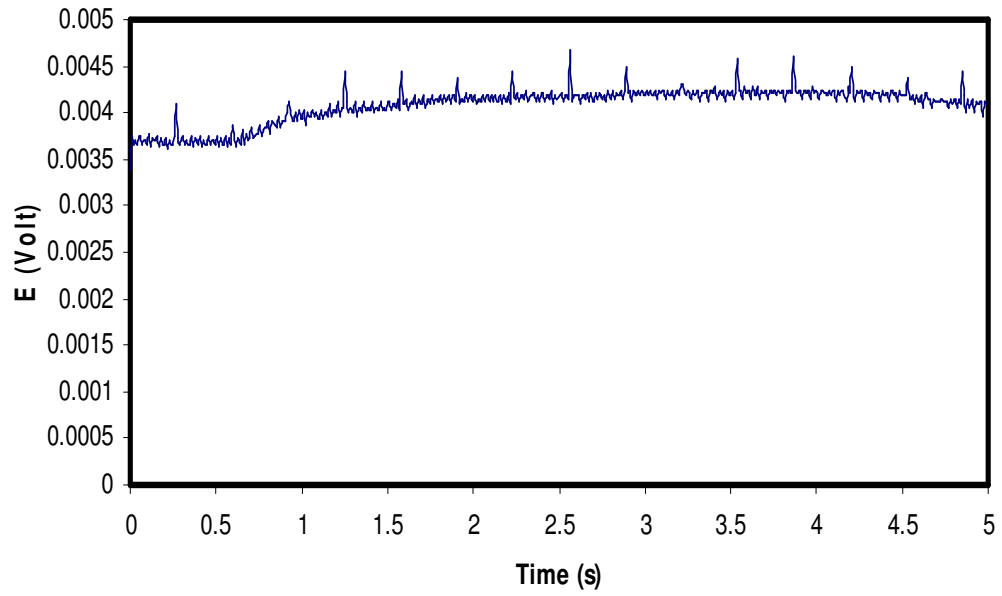


Fig. 6.1 Sample plot of output of TSBS for weak heated jet

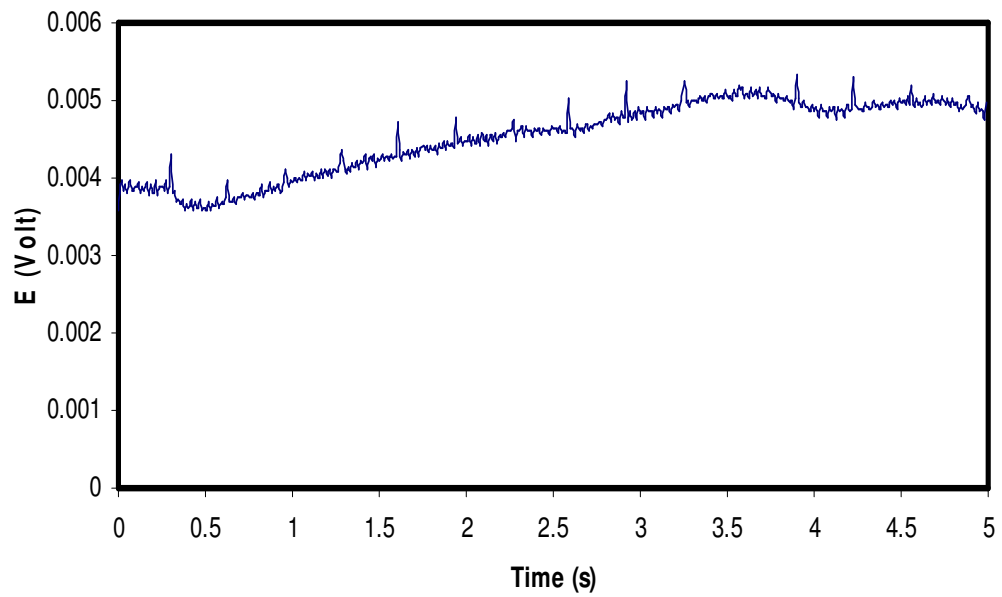


Fig. 6.2 Sample plot of output of TSBS for strong heated jet

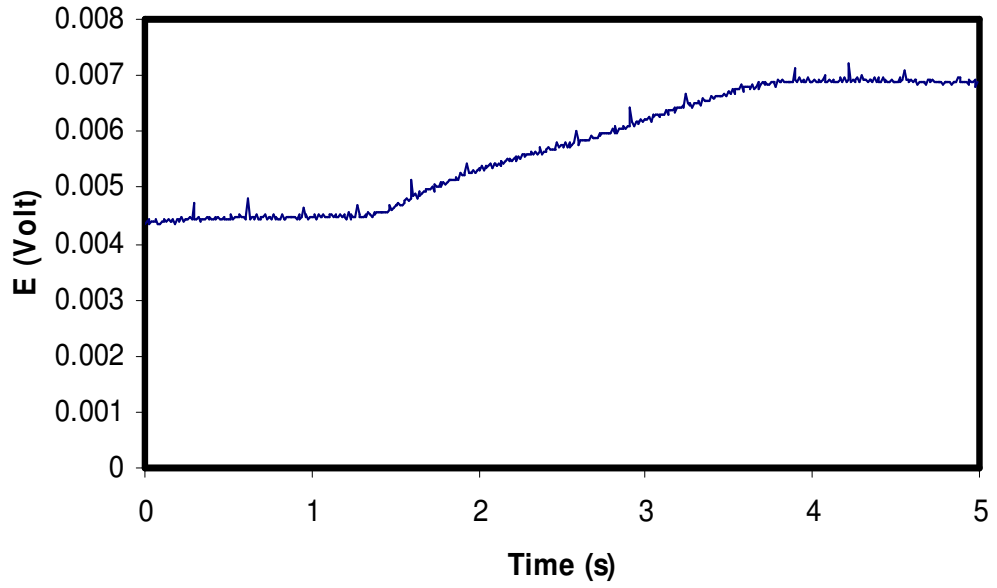


Fig. 6.3 Sample plot of output of the 3-layered TSBS for application of ice

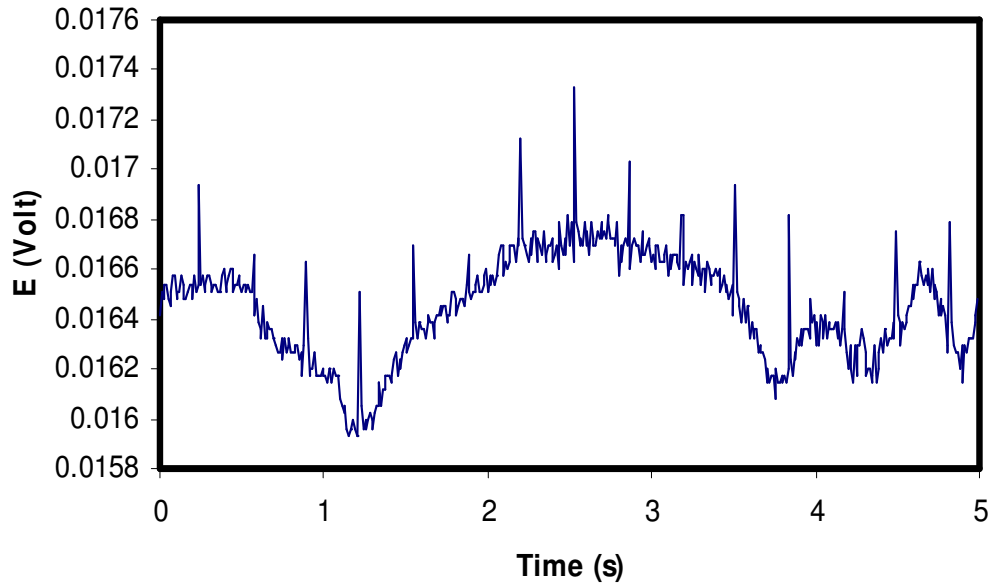


Fig. 6.4 Sample plot of output of the 3-layered TSBS for strong heated jet

The response of the three-layered TSBS to the application of the heated jets was erratic as seen in Fig. 6.4. But the response of the test sensor to the application of ice followed the expected trend and the output was very pronounced. Due to the lack of a reference sensor to measure the amount of heat flux going into the three-layered TSBS, a quantitative assessment of the sensitivity of the gage was impossible. The final conclusion on the TSBS is that the magnitude of the output signal from the 46-layered TSBS was no greater than the output from the 3-layered TSBS. Therefore, this concept was not pursued further.

6.2 HTHFS with Three Brass/Steel Junctions

The first prototype of the HTHFS was tested for its heat flux response using ice. The results from those experiments are given below.

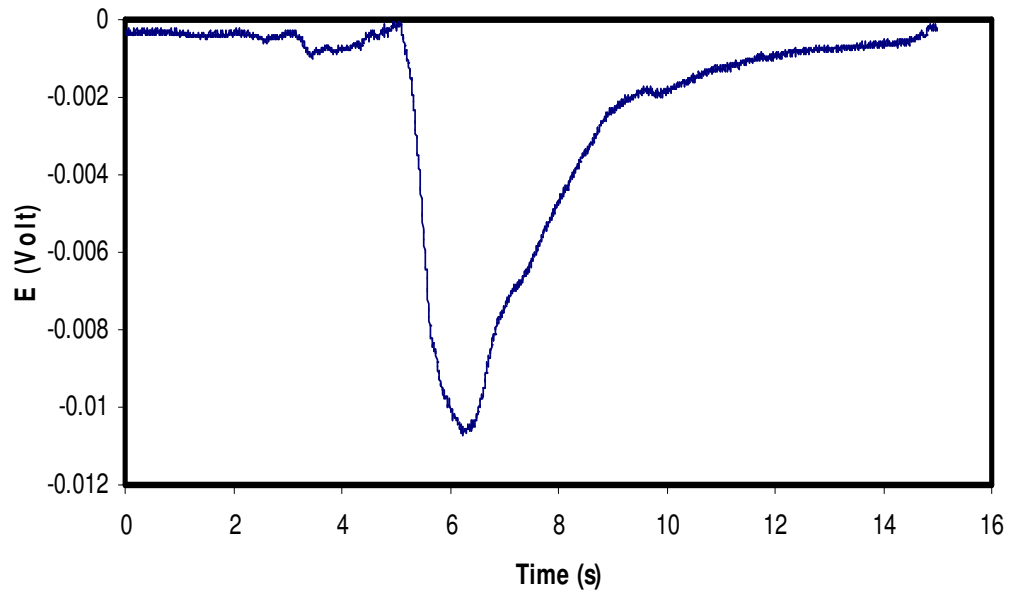


Fig. 6.5 Sample plot of output of the 3-junction HTHFS for medium heat flux

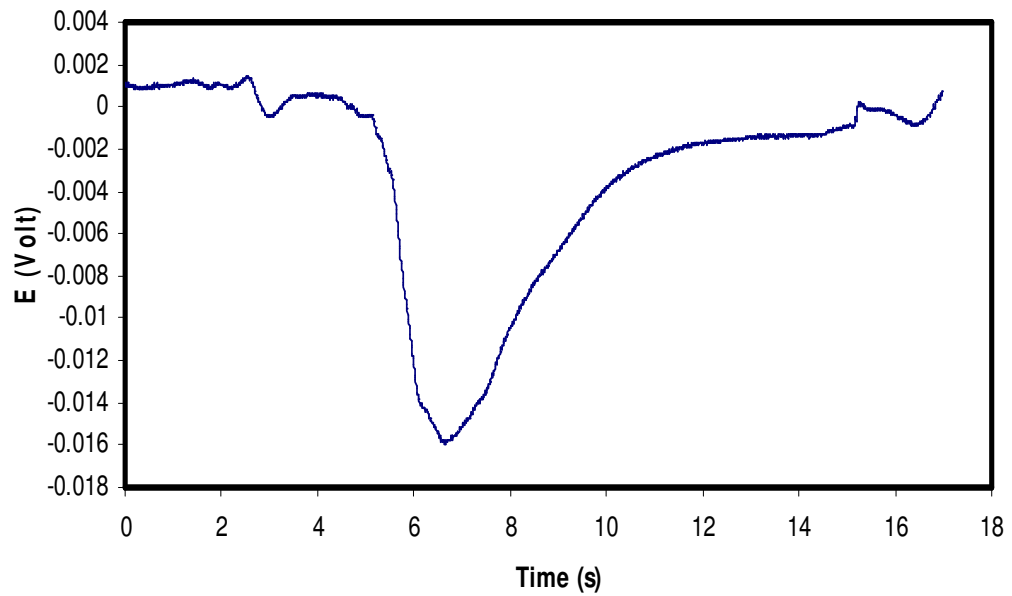


Fig. 6.6 Sample plot of output of the 3-junction HTHFS for strong heat flux

From the heat flux data from the 3-junction HTHFS shown in Fig. 6.5 and 6.6, it was evident that the heat flux through the sensor reached its maximum in about 1s, which corresponds with analytical calculations for the time constant of the brass/steel combination. The signal reached its maximum and decayed exponentially giving rise to a distinct shark fin shape. This was as expected because the other surface of the sensor was in contact with an insulator (Lexan plastic box) causing stagnation of the heat flux. This results in a uniform temperature profile across the sensor causing any thermoelectric signal caused by the thermal gradient to die out. From Fig. 6.5 and 6.6, it was evident that the output increased with increasing heat flux. The heat flux variations were not calculated due to lack of a reference sensor.

6.3 HTHFS with 10 junctions

The response of the HTHFS and the HFM for the application of a weak, medium, and strong heated jet along with the signals from the two thermocouples are given in Fig. 6.9 – 6.20.

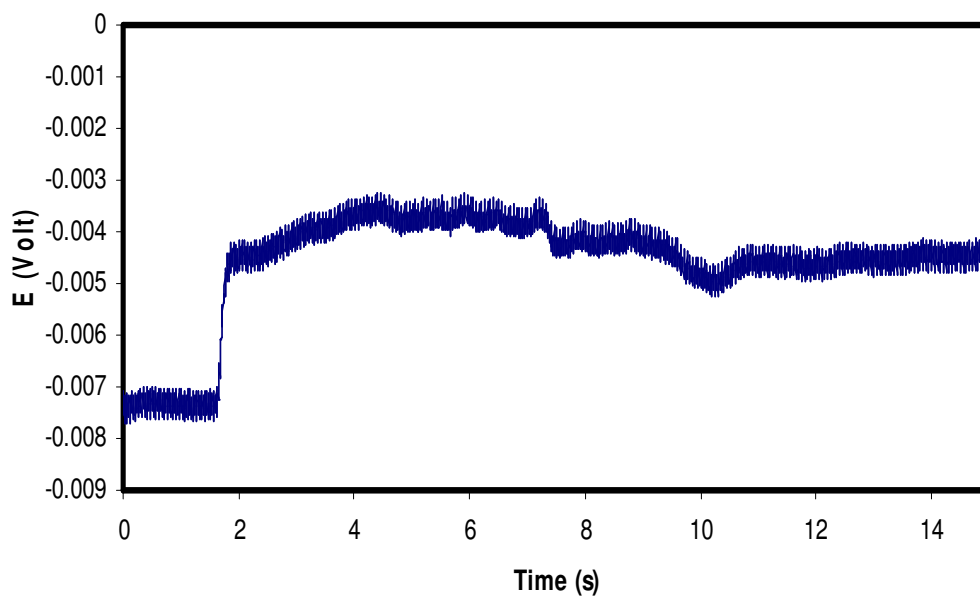


Fig. 6.7 Sample plot of HTHFS output for application of a heated weak jet

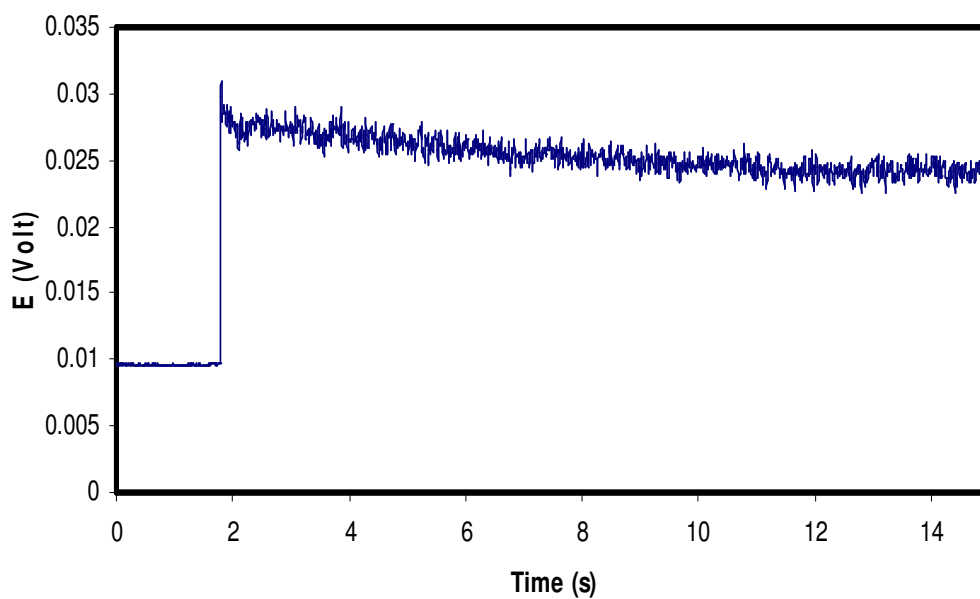


Fig. 6.8 Sample plot of HFM output for application of heated weak jet

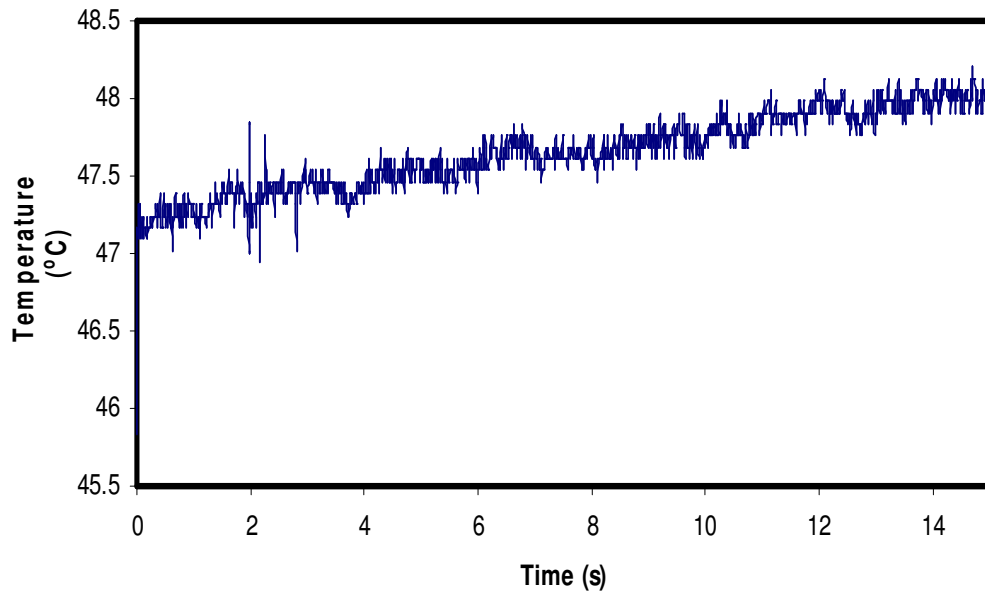


Fig. 6.9 Sample plot of air temperature of the heated weak jet

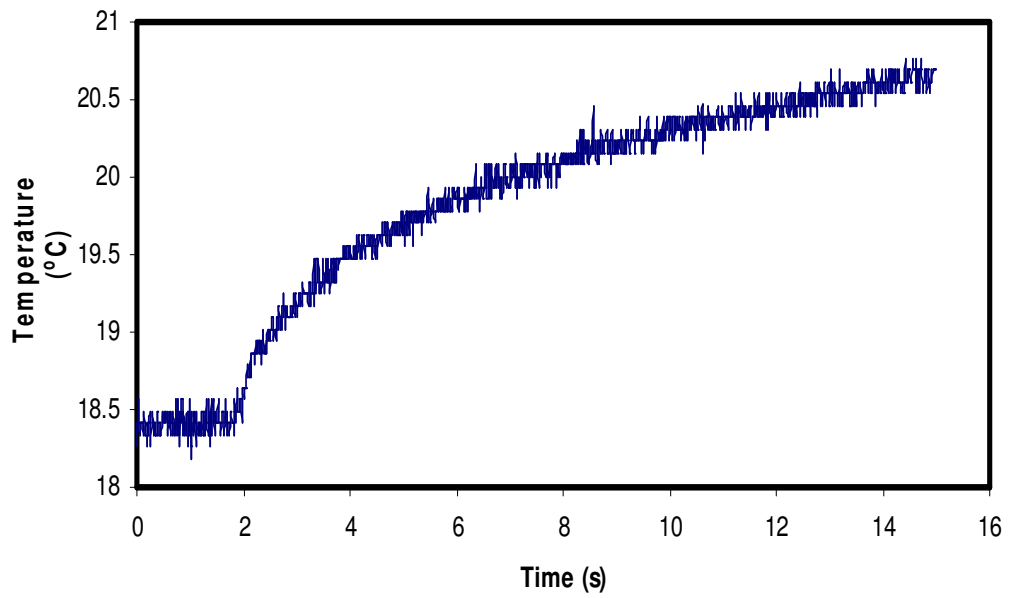


Fig. 6.10 Sample HFM plate temperature for low heat flux run

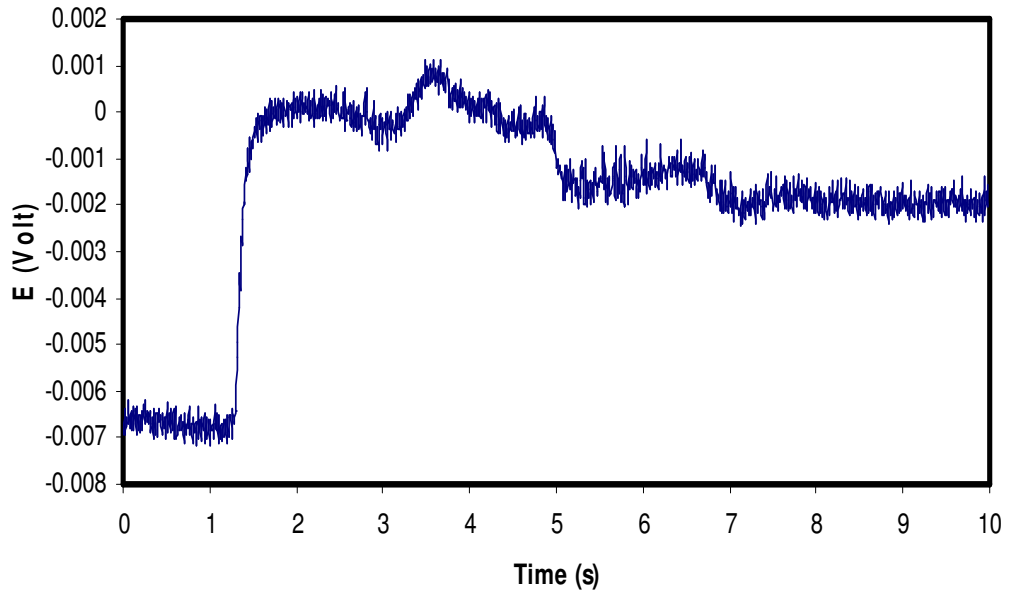


Fig. 6.11 Sample plot of HTHFS output for medium heat flux run

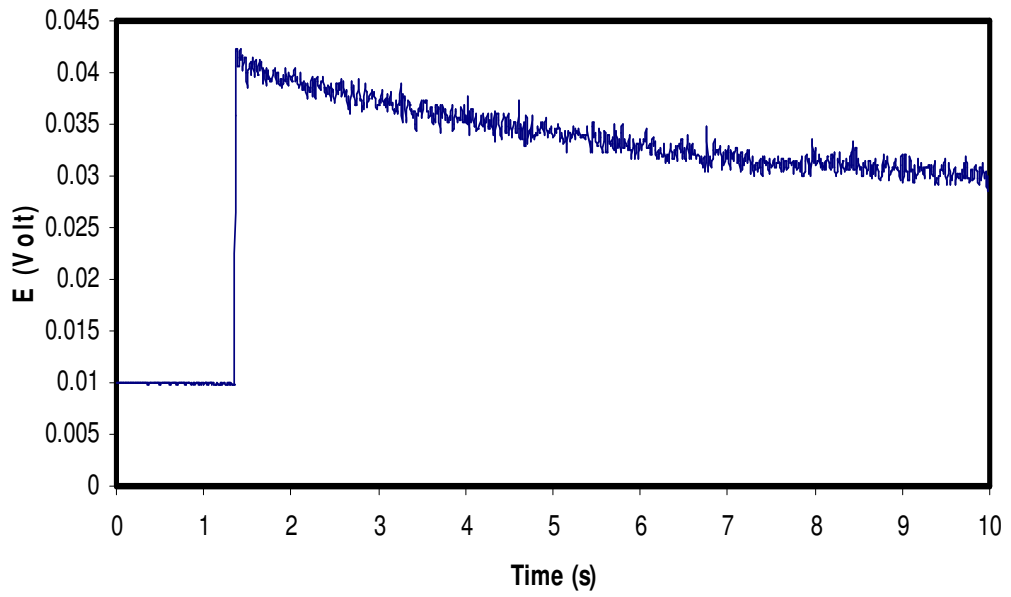


Fig. 6.12 Sample plot of HFM heat flux data for medium heat flux run

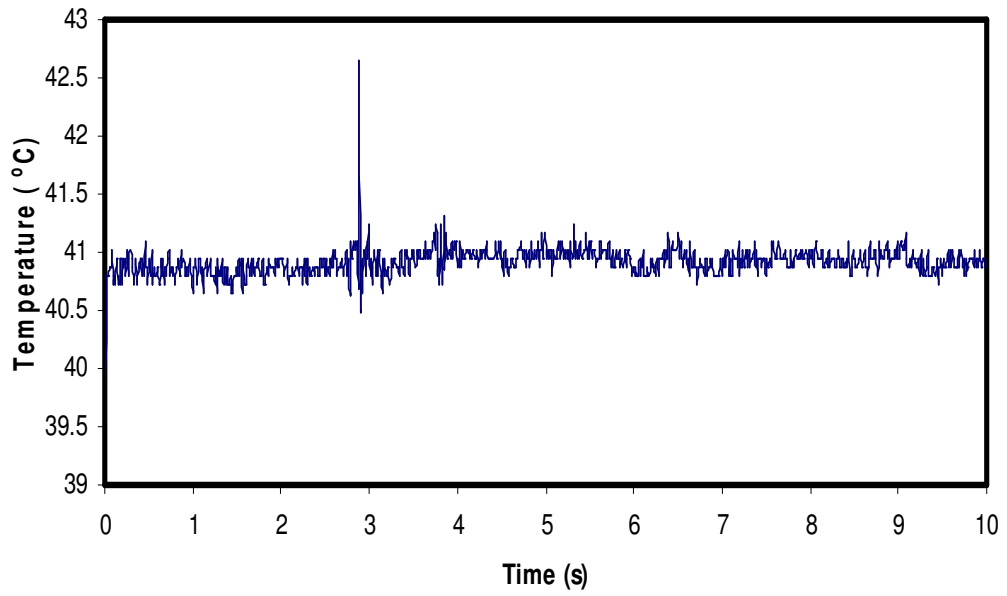


Fig. 6.13 Sample plot of air temperature of the medium strength jet

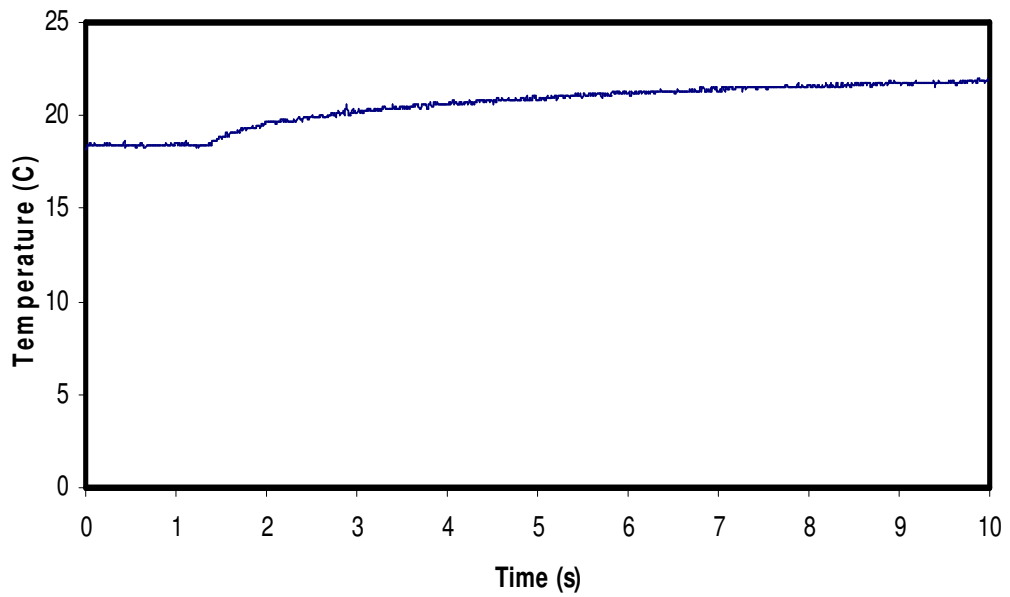


Fig. 6.14 Sample HFM plate temperature for medium heat flux run

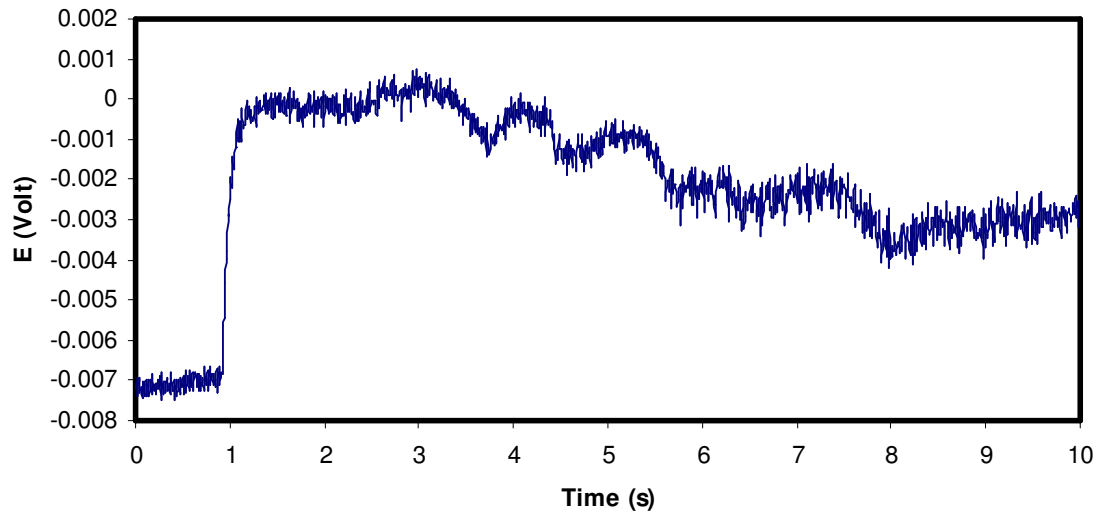


Fig. 6.15 Sample plot of HTHFS output for high heat flux run

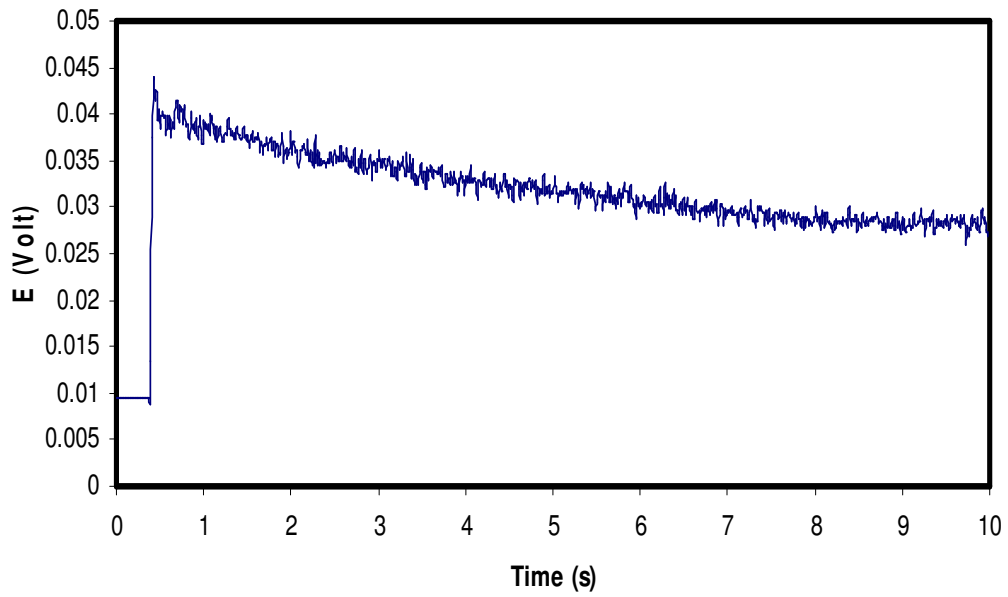


Fig. 6.16 Sample plot of HFM heat flux data for high heat flux run

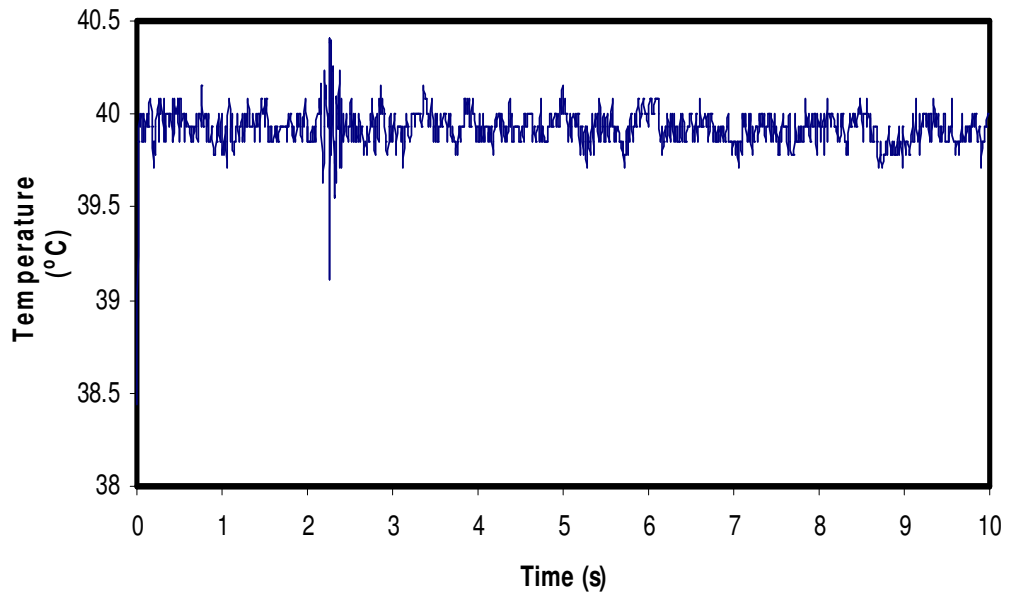


Fig. 6.17 Sample plot of air temperature of the strong jet

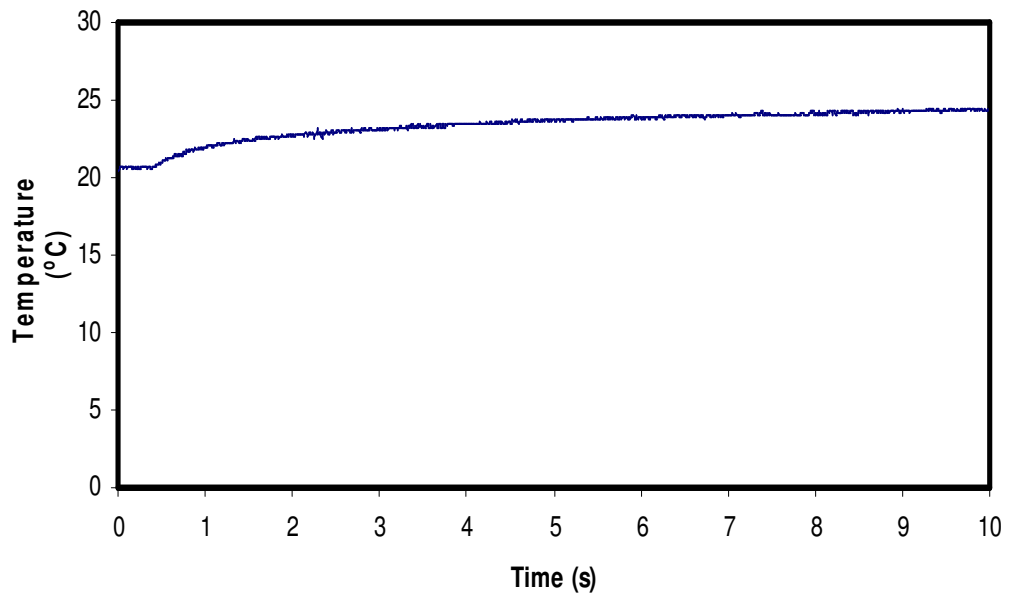


Fig. 6.18 Sample HFM plate temperature for high heat flux run

The HTHFS output signal increased in magnitude for increasing levels of heat flux as shown in Fig. 6.7, 6.9, and 6.13. Although the signal showed a distinct trend, there was considerable amount of noise present in the signal. The noise that was a source of concern is the waviness in the signal. A reasonable explanation for the presence of this noise in the HTHFS is the imperfect contact between the sensor and the surface of the aluminum plate on which it is mounted. In addition, there was a thin plastic film present between the bottom surface of the sensor and the plate. There was a tendency for the plastic film to curl up underneath the sensor causing thick spots randomly between the sensor and the plate. This was seen when the mounted sensor was removed and examined. But this was not a source of concern because only the average values of the output signal strength is used, thus alleviating the effect of the noise.

The signal from the HFM in response to the applied heat flux is shown in Fig. 6.8, 6.12, and 6.16. The response of the sensor was almost instantaneous, which shows that the air jet aimed at the HFM was well positioned. The plots show an instantaneous maximum and a slow decay to a steady state value after that. The maximum value occurs when the heated jet first impinges on the HFM. This is when the temperature difference between the heated air and the HFM is at its maximum and after a while the HFM surface temperature reaches a steady equilibrium temperature. This behavior is seen in the HTHFS also. The noise in the HFM signal, which shows up as periodic oscillations over a mean value is actually the fluctuation in the local heat flux caused by turbulence in the jet. This knowledge was gained from previous experience with the HFM. The HFM was able to record these variations in the heat flux because of its small time constant.

The temperature of the air jet and the surface temperature of the HFM mounted plate are given in Fig. 6.9, 6.10, 6.13, 6.14, 6.17, and 6.18. The air temperature plot shows a distinct noise peak between 2 and 3 seconds. This could be due to some disturbance caused in the airflow due the physical removal of the wooden blocks placed between the nozzles and the sensors. Also, the thermocouple was taped to the outer

surface of the nozzle with the reading junction bent into the nozzle. This gives it some room to flutter. This may also be the cause of the problem.

The HFM plate surface temperature always rises about 2°C after the air jet starts to impinge in it. This is as expected. The signal is level up to a certain point indicating the plate's temperature before the heat flux was applied. At the point where the physical blockages are removed, the surface temperature rose steadily to a new higher value. As the plate surface temperature rises, the temperature difference between the air jet and the plate decreases and thereby reducing the amount of heat flux into the plate by convection as seen in the HFM and the HTHFS signal.

6.4 Heat Transfer Coefficient

The average heat flux through the two sensors by convection was estimated using the voltage signal from the HFM. The heat flux through the HTHFS was also expected to be the same as the heat flux through the HFM. With the average heat flux calculated, the next step was to calculate the average heat transfer coefficient of the heated jets incident on the sensors. The plots of the average heat transfer coefficient over time are shown in Fig. 6.19, 6.20, and 6.21.

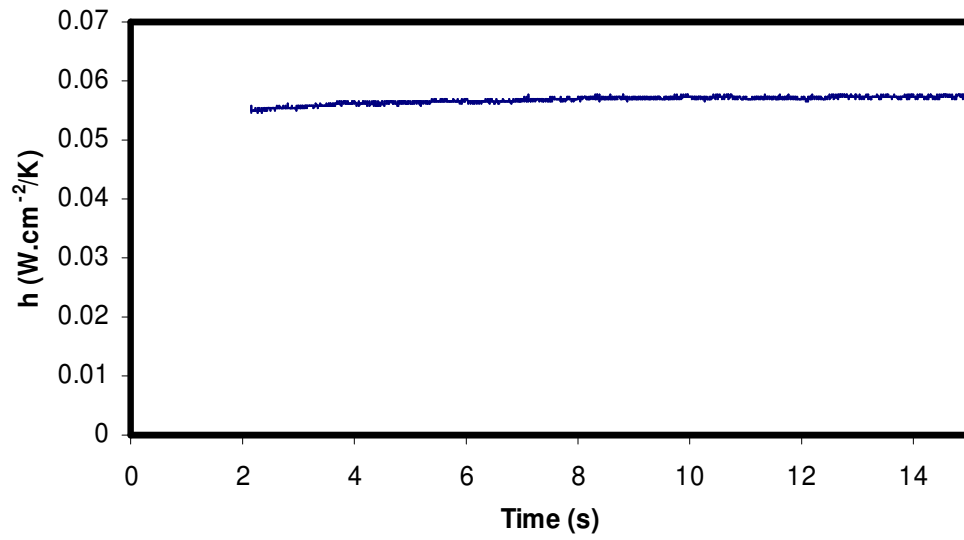


Fig. 6.19 Sample plot of the heat transfer coefficient of the heated weak jet

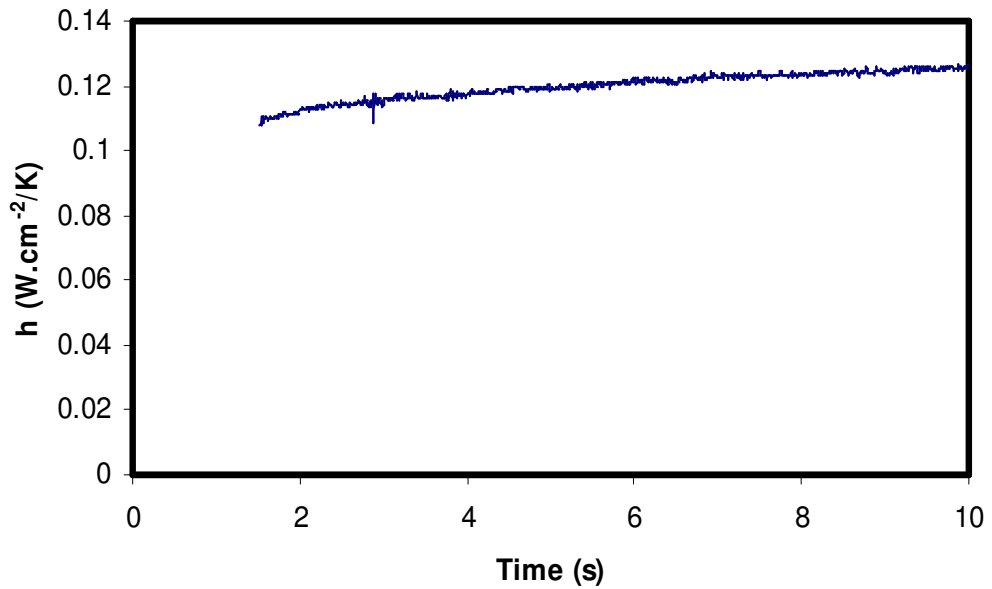


Fig. 6.20 Sample plot of the heat transfer coefficient of the heated medium jet

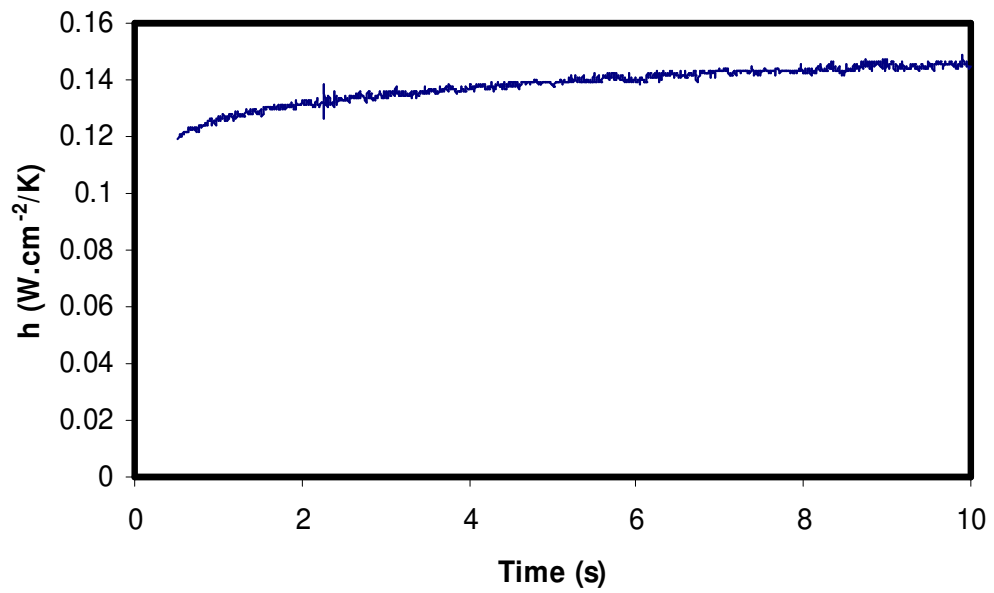


Fig. 6.21 Sample plot of the heat transfer coefficient of the heated strong jet

The average heat transfer coefficients show a steady average value over time and as expected the average heat transfer coefficient increases with increase in the airflow rate of the heated jet. From Fig. 6.21 and 6.22, it can be seen that the average heat transfer coefficient increases more than twofold from $0.055 \text{ W/cm}^2\cdot\text{°C}$ for the weak jet to $0.12 \text{ W/cm}^2\cdot\text{°C}$ for the medium jet. However, the increase in the average heat transfer coefficient value in going from the medium jet to the strong jet is small ($\sim 0.01 \text{ W/cm}^2\cdot\text{°C}$). This indicates that the airflow was probably choked in the nozzle in going from the medium jet to the strong jet. The values estimated for the average heat transfer coefficient were reasonable ($\sim 550\text{-}1300 \text{ W/m}^2\cdot\text{°C}$).

Chapter 7.0

Discussion

7.1 Sensitivity of the HTHFS

The raw data from the calibration tests of the HTHFS were presented in the previous chapter. The sensitivity of the HTHFS versus time was plotted for the low, medium, and high heat flux run in Fig. 7.1, 7.2, and 7.3 respectively.

The plots in Fig. 7.1, 7.2, and 7.3 show that the sensitivity of the HTHFS fluctuated around some mean value. Since the sensitivity of the HFM is $100 \mu V/(W/cm^2)$ it is reasonable to expect that the sensitivity of the test sensor will be between 20 and $25 \mu V/(W/cm^2)$ just by looking at the plots. The actual sensitivity of the HTHFS will be estimated using the heat flux data later.

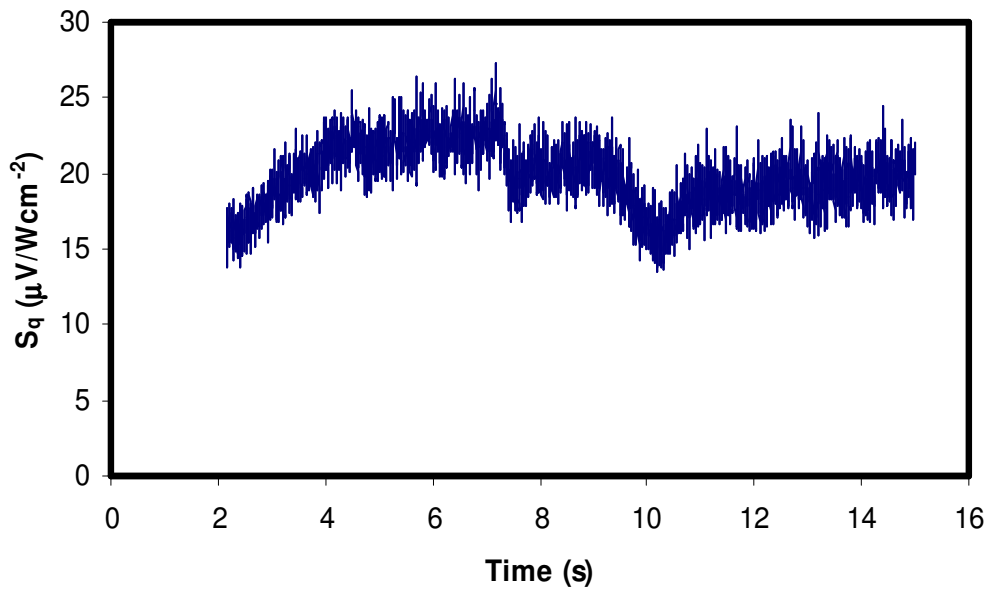


Fig. 7.1 Sample plot of HTHFS sensitivity for low heat flux run

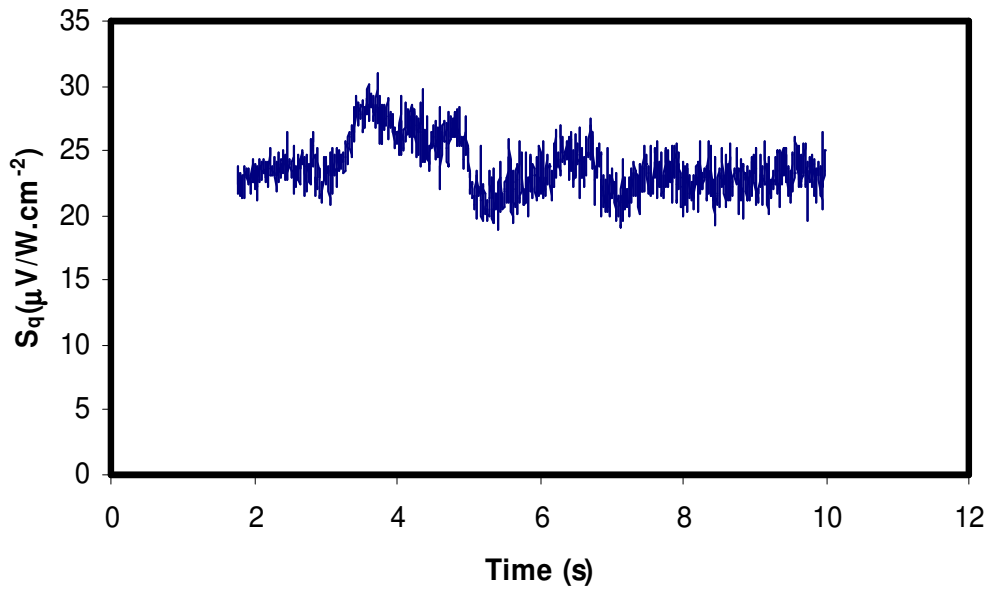


Fig. 7.2 Sample plot of HTHFS sensitivity for medium heat flux run

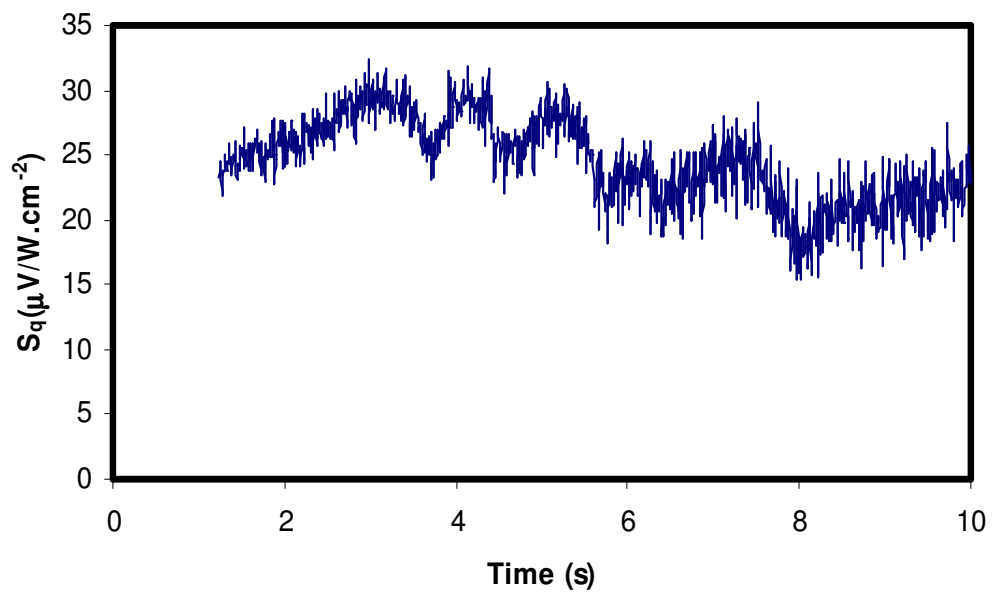


Fig. 7.3 Sample plot of HTHFS sensitivity for high heat flux run

7.2 Measured Sensitivity of the HTHFS

The ultimate goal of this calibration test is to determine the sensitivity of the HTHFS. Using the procedures outlined in chapter 4, the sensitivity of the HTHFS was calculated using the data collected from each run. The values computed for the sensitivity of the HTHFS along with the average heat transfer coefficient for each run are given in Table 7.1.

Table 7.1 Sensitivity values from each run

Run	Heat Transfer Coefficient (W/cm ² .°C)	Sensitivity (μ V/(W/cm ²))
1	0.0569	19.8
2	0.0518	15.7
3	0.0547	15.8
4	0.0510	16.4
5	0.0493	16.3
6	0.0509	19.8
7	0.121	28.8
8	0.120	23.8
9	0.112	22.2
10	0.109	22.2
11	0.105	20.3
12	0.103	22.3
13	0.138	24.6
14	0.135	18.1
15	0.132	19.6
	Average- 0.0926	20.38

7.3 Uncertainty Analysis

There are many errors in these measurements that would cause an uncertainty in the value obtained for the HTHFS sensitivity. The sources of error are given below in Table 7.2. One approach to assess the uncertainty in the value obtained for the sensitivity of the HTHFS is to quantify the uncertainty caused by each of the individual sources and then calculate the root mean square of these values. The individual error values and the total error are given for each run in Table 7.3. The error due to radiation was calculated by calculating the heat flux due to radiation using equation 7.1 first.

$$q''_{radiation} = \epsilon \sigma (T_{HTHFS}^4 - T_{surr}^4) \quad (7.1)$$

where ϵ is the emissivity, σ is the Stefan-Boltzmann constant, T_{HTHFS} is the surface temperature of the HTHFS, and T_{surr} is the room temperature. T_{HTHFS} was assumed to be the same as the HFM plate temperature and T_{surr} was measured to be 18.3°C. The error was calculated by dividing this value by the convection heat flux value obtained from the HFM output. The error due to radiation was calculated for $\epsilon = 0.9$.

The error due to the assumption of similar heat transfer coefficients (σ_h) was assumed to be 2%. A better way to estimate this error would be to measure the heat transfer coefficient of both air-jets. The error caused by the amplifier was given as $\pm 1.5\%$ for a gain of 100 in the Vatell Amp-6 amplifier data sheet.

The error in the calculated mean of the sensitivity (S_q) in each run was estimated using the following method: After the sensitivity versus time plot had been made for each run, the average low value and the average high value was computed. The difference between these two values gave the range of the error in the mean. The uncertainty in the mean was estimated as 25% of this range.

The other approach was to recognize that the sample is a single valued quantity. For samples that have single valued quantities, the standard deviation in the mean is estimated as the uncertainty in the measurement of the sample. For expanded uncertainty, the standard uncertainty value is multiplied by the appropriate coverage factor k. The standard deviation of the mean for n samples is calculated using equation 7.2.

$$s_m = \frac{1}{n(n-1)} \sum_{i=1}^N (X_i - \mu)^2 \quad (7.2)$$

where X_i = Sensitivity value, μ = mean of the sensitivity values. Using the Student's t-distribution, the coverage factor (k) for corresponding to 15 samples and 95% confidence is found to be 2.14. So, the 95 % confidence interval on the mean of the sensitivity values was determined to be $2.05 \mu \text{ V}/(\text{W}/\text{cm}^2)$. The uncertainty for the sensitivity was determined to be $\pm 10\%$. The results from this analysis are presented in Table 7.4.

Table 7.2 Sources of uncertainty in the calibration results

Error Type	Source
Precision	Error in the voltmeter
Precision	Error in the amplifiers
Bias	Assumption of same heat transfer coefficient on both sides
Bias	Error due to radiation effects
Precision	Error in the estimation of the mean of the sensitivity in each run

Table 7.3 Error propagation in the sensitivity value of the HTHFS

Run	$\sigma_{\text{voltmeter}}$ (%)	$\sigma_{\text{radiation}}$ (%)	σ_h (%)	σ_{amp} (%)	σ_{mean} (%)	σ_{total} (%)
1	5.45	0.046	2	1.5	7.75	9.80
2	7.79	0.07	2	1.5	13.82	16.06
3	7.76	0.066	2	1.5	14.68	16.79
4	7.92	0.082	2	1.5	16.47	18.45
5	8.71	0.094	2	1.5	12.92	15.78
6	7.24	0.098	2	1.5	12.49	14.65
7	2.31	0.027	2	1.5	8.72	9.36
8	3.09	0.047	2	1.5	6.64	7.74
9	4.15	0.079	2	1.5	8.09	9.43
10	4.6	0.099	2	1.5	10	11.29
11	5.56	0.114	2	1.5	11.32	12.86
12	4.09	0.08	2	1.5	7.51	8.91
13	3.2	0.114	2	1.5	10.84	11.58
14	5.06	0.124	2	1.5	16.34	17.29
15	3.77	0.096	2	1.5	13.32	14.07

Table 7.4 Sensitivity of the HTHFS and average heat transfer coefficient

Heat Transfer Coefficient (W/cm ² .°C)	Sensitivity (μ V/(W/cm ²))	Standard Deviation	Number of sample (n)
0.0569	19.8	2.38	1298
0.0518	15.7	3.58	1375
0.0547	15.8	2.98	781
0.0510	16.4	3.66	878
0.0493	16.3	3.36	850
0.0509	19.8	3.76	800
0.121	28.8	2.54	829
0.120	23.8	2.16	836
0.112	22.2	2.58	765
0.109	22.2	2.4	813
0.105	20.3	2.84	824
0.103	22.3	2.56	778
0.138	24.6	3.43	868
0.135	18.1	3.92	801
0.132	19.6	3.26	850
Average = 0.0926	20.38 \pm 2.05		

7.4 Plot of sensitivity versus heat transfer coefficient (h)

A plot of the HTHFS sensitivity versus the heat transfer coefficient (h) calculated from each run is given in Fig. 7.4. The error bars on the data points indicate the uncertainty in each calculated sensitivity value. The data points seem to exhibit a linear trend thus hinting at the possibility of a linear relationship between the sensitivity of the HTHFS and the heat transfer coefficient. But after the error bars had been included in the plot, it was clearly seen that the scatter in the data is purely random. Thus the slope of the linear curve fit would be statistically insignificant.

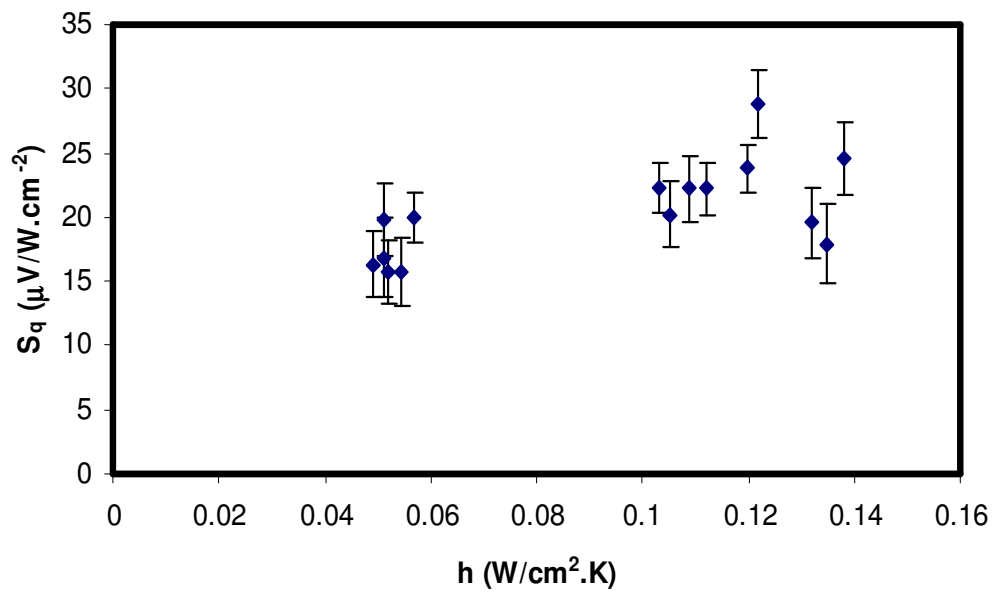


Fig. 7.4 Sensitivity of HTHFS versus heat transfer coefficient (h)

7.5 Theoretical Estimation of HTHFS Sensitivity

The theoretical sensitivity of the HTHFS was calculated by combining the expression for voltage output from thermopile circuits and the expression for heat flux through conduction. The theoretical output for a thermopile circuit having N junctions is given by equation 7.2. Since the voltage is generated between two junctions, N represents the number of junction pairs in the HTHFS.

$$E = NS_T\Delta T \quad (7.2)$$

The heat flux by conduction through the sensor is given by equation 7.3. Dividing equation 7.2 by equation 7.3 gives the theoretical sensitivity of the HTHFS which is given by equation 7.4

$$q'' = k \frac{\Delta T}{\delta} \quad (7.3)$$

$$\text{Sensitivity} = \frac{E}{q''} = \frac{N S_T \delta}{k} \quad (7.4)$$

where S_T is the Seebeck coefficient of brass/steel pair, δ is the thickness of the material in the direction of the heat flux, and k is the thermal conductivity of the material.

The Seebeck coefficient (S_T) of brass/steel thermocouple was determined in a separate experiment (Appendix B). The value of S_T was found to be approximately $12 \mu\text{V}/^\circ\text{C}$. The thickness δ was measured between two opposing junctions as shown in Fig. 7.5. The value of δ was measured to be 0.32 cm. The value of 'k' was determined by taking the average of the tabulated values of 'k' for brass and steel. The average value of 'k' was calculated to be 93.5 W/m-K. Substituting these values into equation 7.4 gave a heat flux sensitivity value of $20.5 \mu\text{V}/(\text{W}/\text{cm}^2)$.

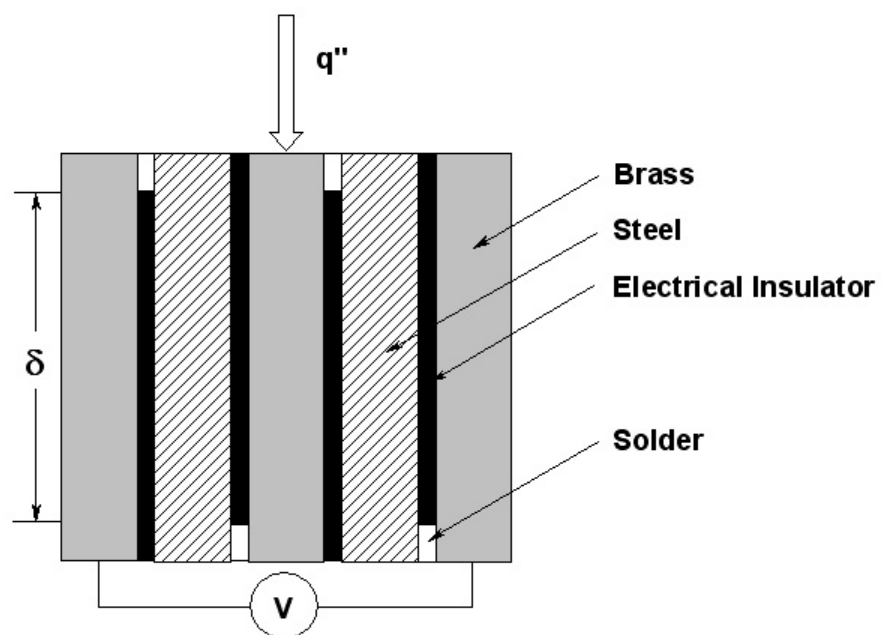


Fig. 7.5 Thickness ' δ ' of the HTHFS

Chapter 8.0

Conclusions and Recommendations

8.1 Conclusions

The calibration tests done on the HTHFS was to verify if the thermopile design of the new heat flux sensor works. One of the main improvements of the new heat flux gage design is that the gage does not use a thermal resistance layer to create a thermal gradient between the upper and lower thermocouple junctions. The thermal resistance layer had been created by the thermocouples themselves. The results from the experiment show that the HTHFS works as expected. The experimentally determined sensitivity ($20.4 \mu\text{V/W.cm}^{-2}$) is close to the theoretically estimated value ($20.5 \mu\text{V/W.cm}^{-2}$) for a thermopile circuit having 10 brass/steel junctions.

This high temperature performance of this sensor is limited by the melting point of the lead in the solder. But the same concept can be pushed further by the use of micro-fabrication techniques for the formation of thermocouple junctions. Since more and more junctions can be built into the thermopile circuit using micro-fabrication techniques, it is reasonable to expect higher sensitivities from these heat flux sensors.

The convection calibration stand that was used in this calibration test was rugged and provided ease of use for the calibration tests. It was easy to change the sides of the HTHFS and HFM mounted plates.

8.2 Recommendations

The following recommendations are suggested for improving the calibration tests:

A new improved method to mount the sensor flush with the surface of the plate while ensuring complete electrical isolation of the sensor from the aluminum plate is advised. This will reduce the errors in the tests further. In future tests, it would be advisable to attach a thermocouple to the surface of the sensor and to the bottom surface of the sensor. Thus the actual surface temperatures of the HTHFS can be determined and the average heat flux value calculated from the HFM data can be used as a comparison of the result. The surface temperature data can then be used to calculate the heat flux through the HTHFS through conduction. Since the heat transfer process is assumed to be steady state, this heat flux value should be the same as the heat flux by convection calculated from the HFM. This would enable to check the accuracy of the data collected from the HTHFS. More convection calibration tests with cooled air are also recommended.

References

- [1] Bennethum, W. H., and Sherwood, L. T. (1998). Sensors for ceramic components in advanced propulsion systems: summary of literature survey and concept analysis. NASA CR-180900.
- [2] Paulon, J., Portat, M., Godefroy, J. C., and Szechenyi, E. (1981). Ultrathin transducers applied to measurements in turbomachines, In *Measurement Techniques in Turbomachines*, Vol. 2. von Karman Institute Fluid Dynamics Rhode St. Genese.
- [3] Godefroy, J. C., Clery, M., Gageaut, C., Francois, D., and Portat, M. (1987). Sputtered alumina layers and platinel thermocouples for high temperature surface thermometers, evaluation of their electrical and mechanical characteristics. ONERA TP 1987-30.
- [4] Neumann, R. D., Erbland, P. J., and Kretz, L. O. (1988). Instrumentation of hypersonic structures: a review of past applications and needs of the future. AIAA Paper No.88-2612.
- [5] Kidd, C. T. (1992). High heat flux measurements and experimental calibrations characterizations. NASA CP3161, pp. 31-50
- [6] Diller, T. E., and Telionis, D. P. (1989). Time-resolved heat transfer and skin friction measurements in unsteady flow. In *Advances in Fluid Mechanics Measurements*, (Lecture Notes in Engineering) (M. Gad-el-Hak, ed.), pp.232-355. Springer-Verlag, Berlin.
- [7] Hager, J. M., Onishi, S., Langley, L.W., and Diller, T.E. (1989). Heat flux microsensors. In *Heat Transfer Measurements, Analysis and Flow Visualization*. (R.K. Shah, ed.), pp. 1-8. ASME, New York.
- [8] Farouk, B., Kim, Y. G., Apelian, D., and Pennucci, J. (1989). Heat flux measurements for metal castings on a spray cooled substrate. In *Heat Transfer Measurements, Analysis and Flow Visualization* (R.K. Shah, ed.) pp. 161-167. ASME, New York.
- [9] Van Dorth. A. C. (1983). Thick film heat flux sensor. *Sensors and Actuators*, **4**, 323-331.

- [10] Hayashi, M., Sakurai, A., and Aso, S. (1986). Measurement of heat-transfer coefficients in shockwave turbulent boundary layer interaction regions with a multi-layered thin film heat transfer gauge. NASA-TM-77958.
- [11] Godefroy, J. C., Gageaut, C., Francois, D., and Portat, M. (1987). Sputtered alumina layers and platinel thermocouples for high temperature surface thermometers, evaluations of their electrical and mechanical characteristics. ONERA TP No. 1986-28.
- [12] Epstein, A.H., Guenette, G.R., Norton, R. J. G., and Cao, Y. (1986). High-frequency response heat-flux gage. *Rev. Sci. Instrum.* **57**, 639-649.
- [13] Hager, J. M., Simmons, S., Smith, D., Onishi, S., Langley, L. W. & Diller, T. E., Experimental Performance of a Heat Flux Microsensor. *ASME Journal of Engineering for Gas Turbines and Power*, **113**, pp. 246-250, 1991.
- [14] Hayes, J., and Rougeux, A. (1991). The application of numerical techniques to model the response and integration of thermal sensors in wind tunnel models. AIAA Paper No. 91-0063.
- [15] Kidd, C.T. (1990). Coaxial surface thermocouples: analytical and experimental considerations for aerothermal heat-flux measurement applications. *Proceedings of the 36th International Instrumentation Symposium*, Pp. 203-211. ISA, Research Triangle Park, NC.
- [16] Divin, N.P., Russian Utility Model Certificate no. 9959, priority of Aug. 10, 1998, *Byull. Polezn. Modeli*, 1999, no. 5.
- [17] Huber, W. M., Li, S. T., Ritzer, A., Bauerle, D., Lengfellner, H., and Prettl, W. (1997). Transverse Seebeck Effect in $\text{Bi}_2\text{Sr}_2\text{CaCu}_2\text{O}_8$. *Appl. Phys. A* **64**, 487-489.
- [18] Mityakov, A. V., Mityakov, V. Yu., Sapozhnikov, S. Z., and Chumakov, Yu. S. (2002). Application of the Transverse Seebeck Effect to Measurement of Instantaneous Values of a Heat Flux on a Vertical Heated Surface under Conditions of Free-Convection Heat Transfer. *High Temperature*, Vol. 40, No. 4, pp. 620-625.
- [19] Zahner, Th., Forg, R., and Lengfellner, H. (1998). *Applied Physics Letters*, Vol. 73, No. 10

Appendix A

HTHFS Output Plots

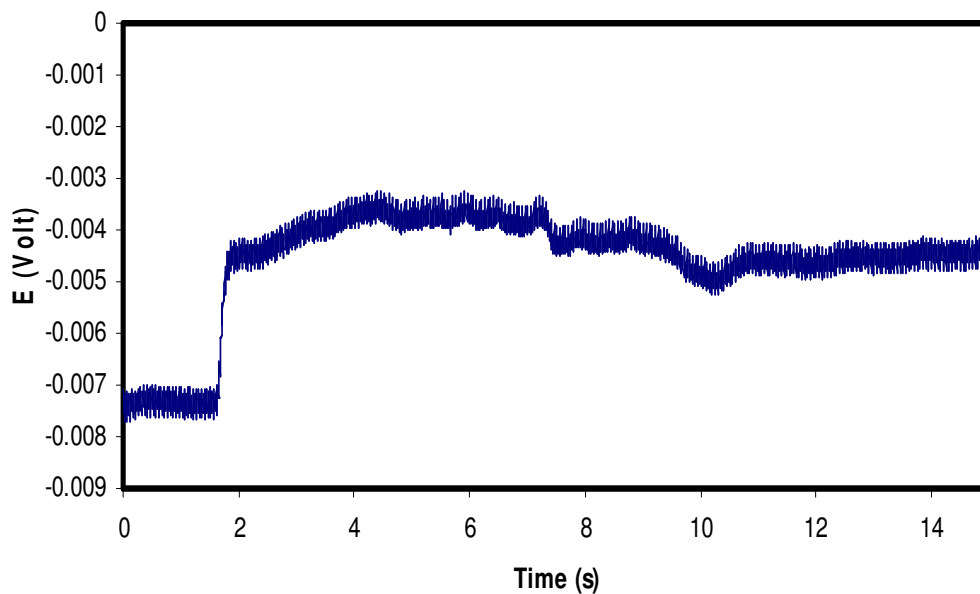


Fig. A.1 HTHFS output from run 1

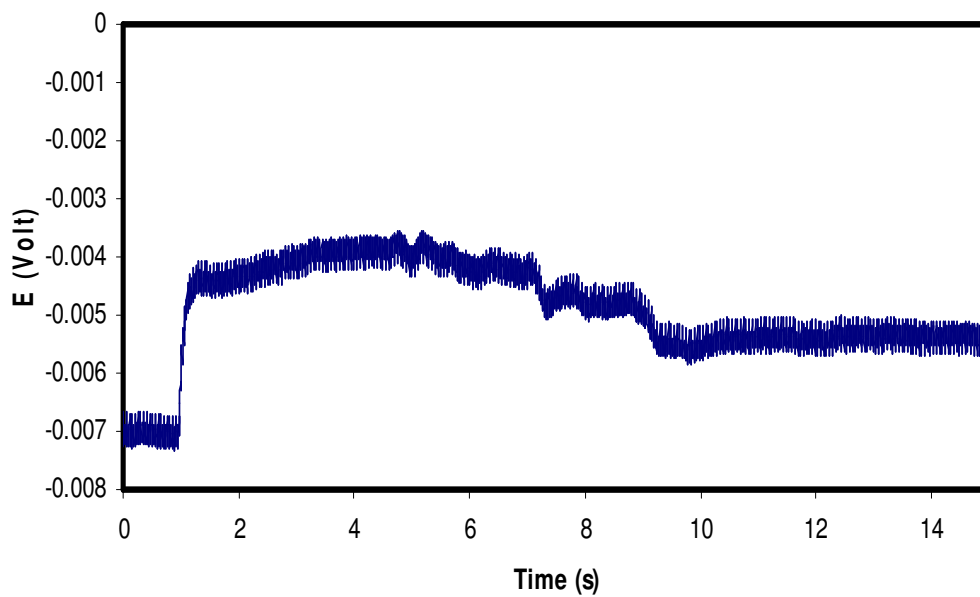


Fig. A.2 HTHFS output from run 2

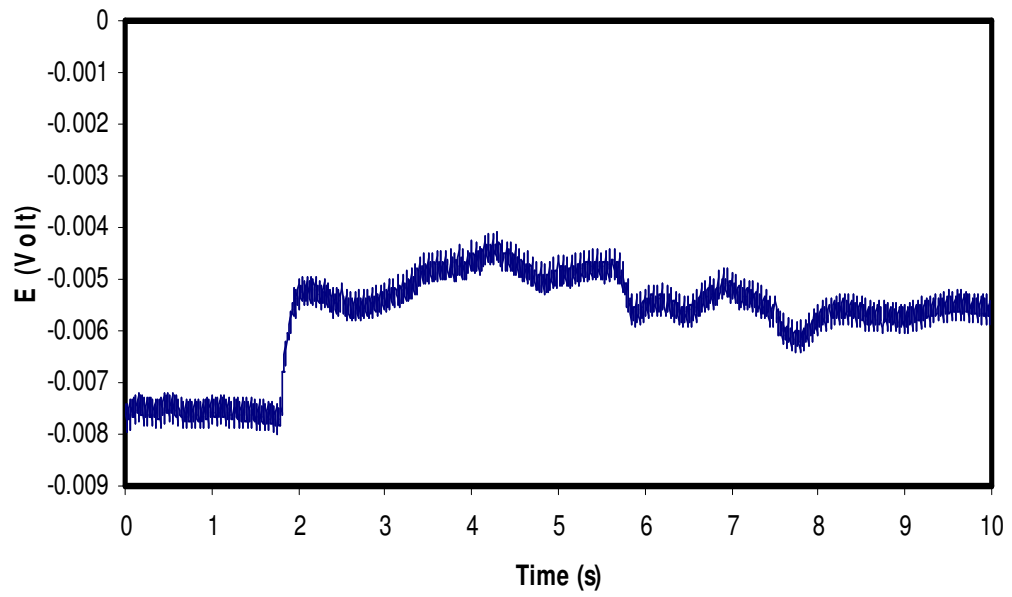


Fig. A.3 HTHFS output from run 3

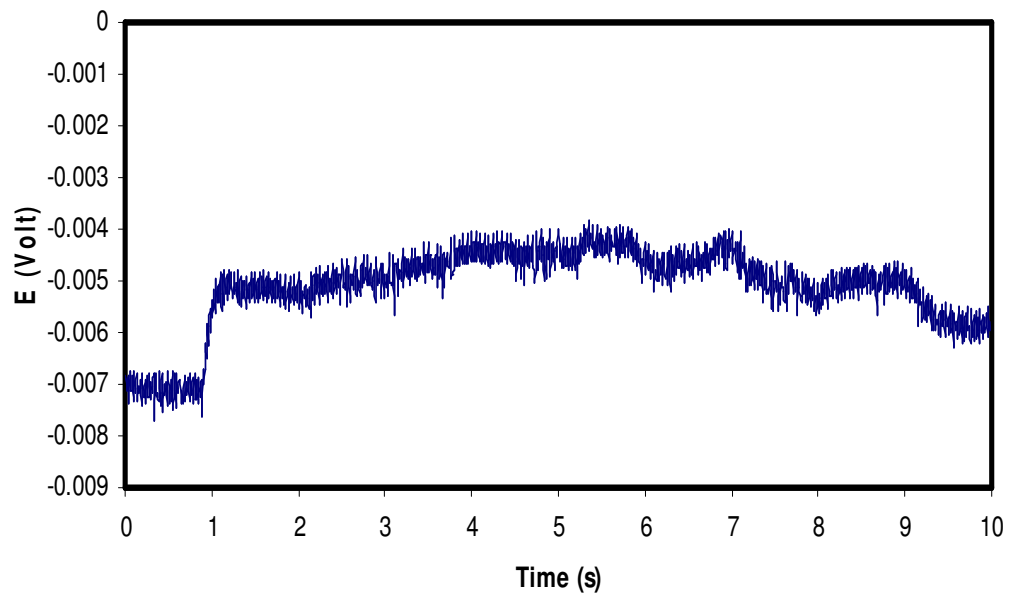


Fig. A.4 HTHFS output from run 4

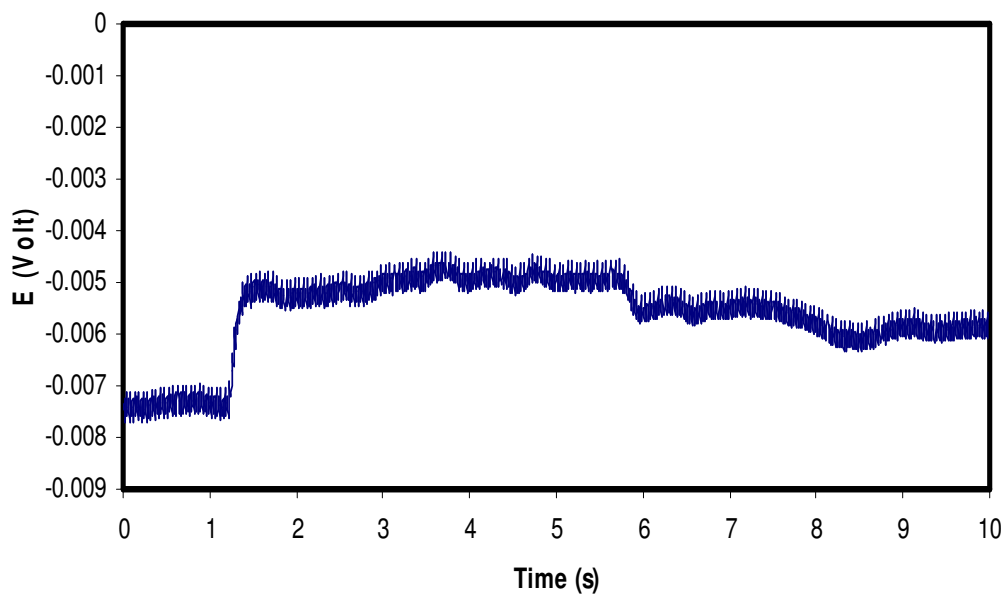


Fig. A.5 HTHFS output from run 5

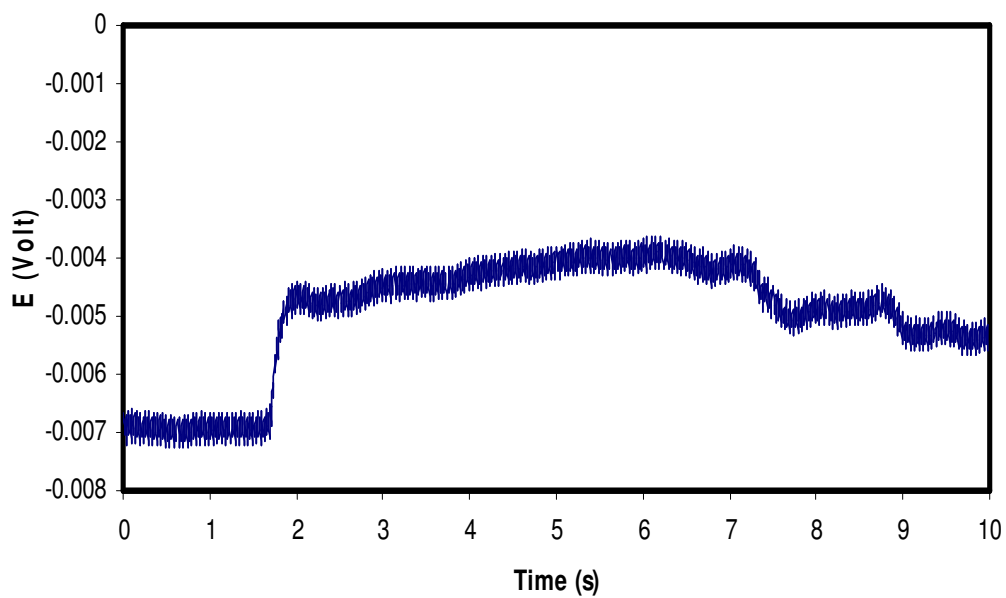


Fig. A.6 HTHFS output from run 6

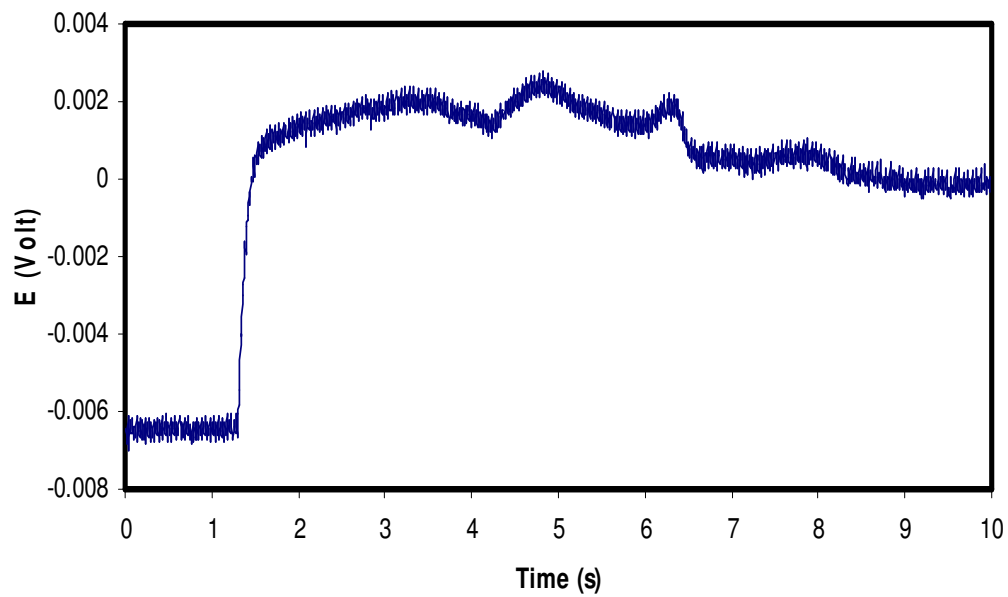


Fig. A.7 HTHFS output from run 7

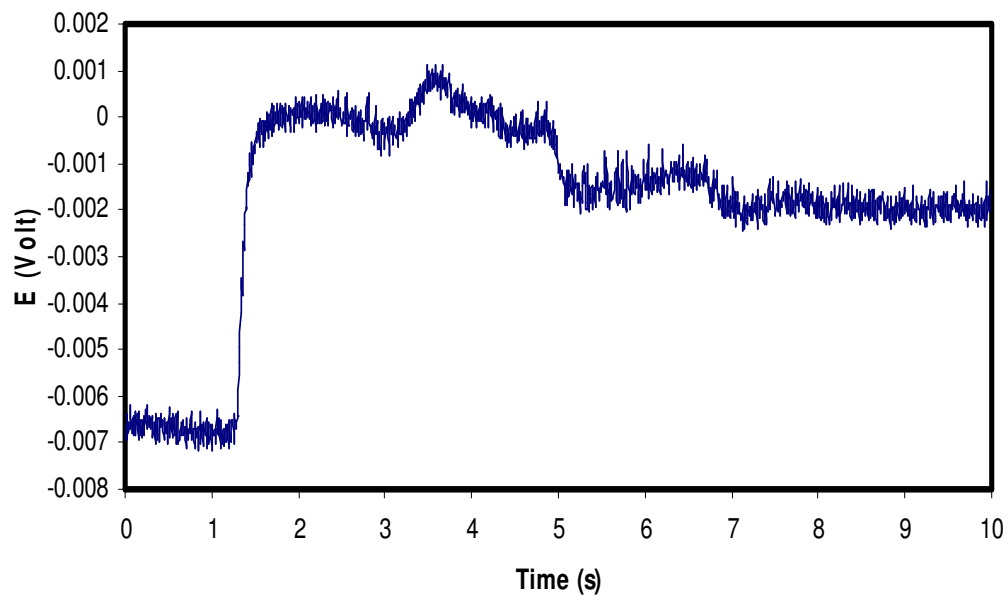


Fig. A.8 HTHFS output from run 8

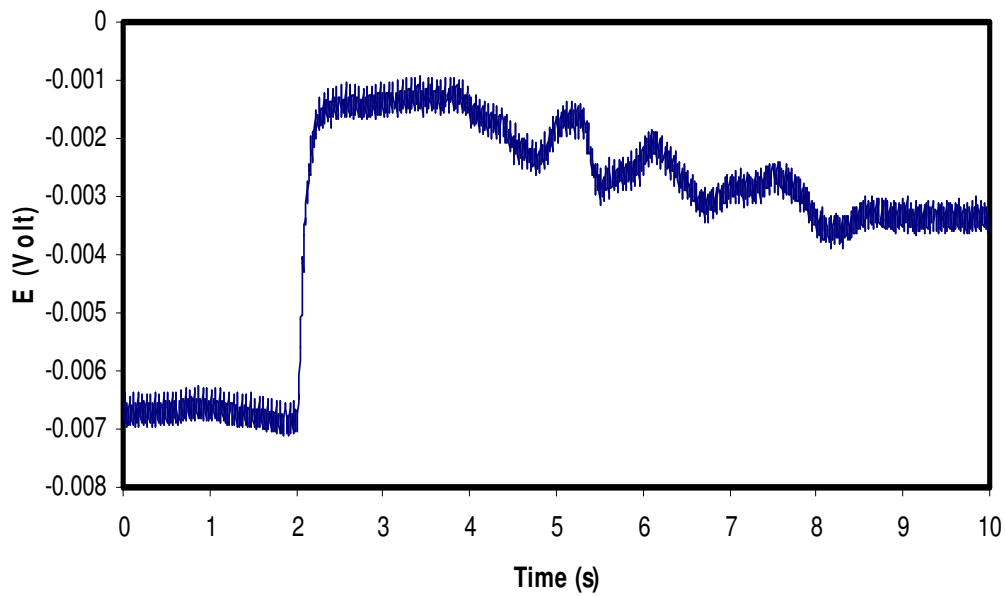


Fig. A.9 HTHFS output from run 9

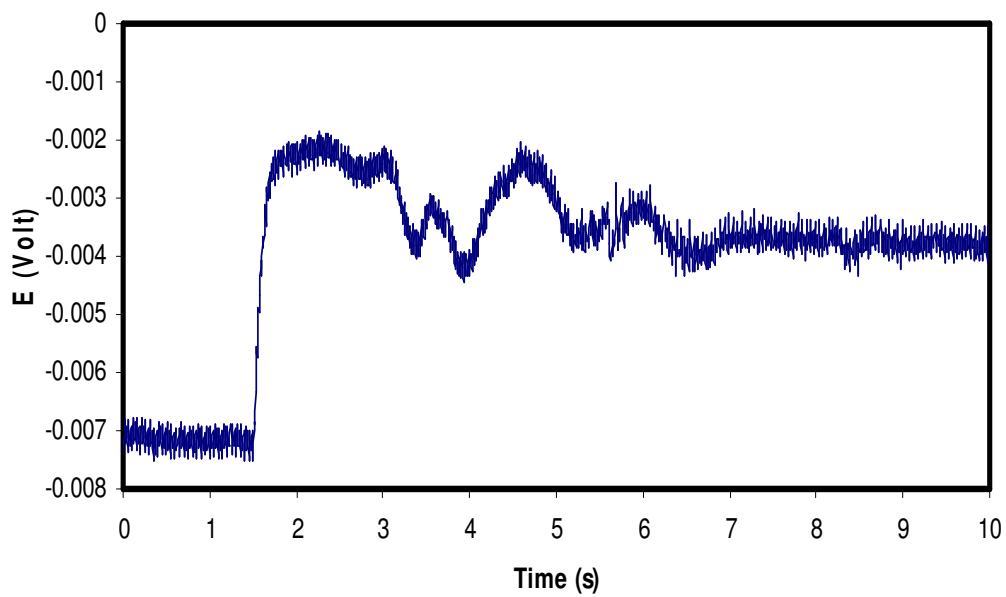


Fig. A.10 HTHFS output from run 10

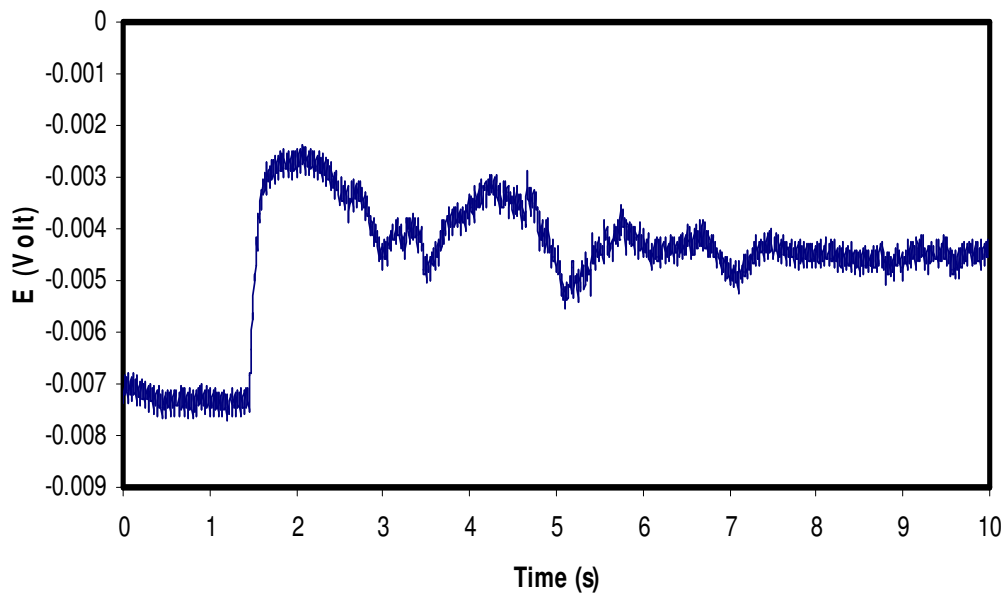


Fig. A.11 HTHFS output from run 11

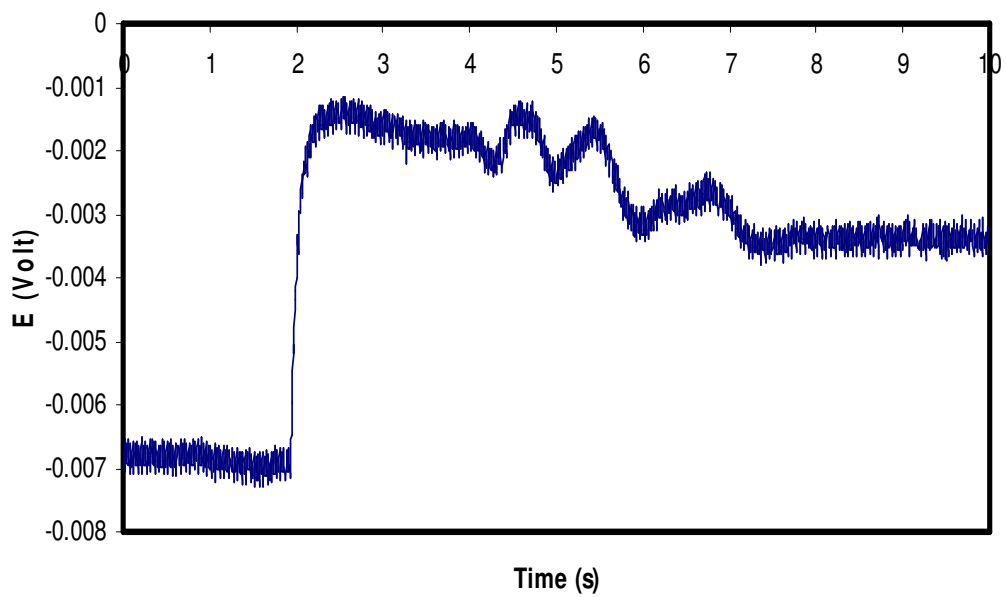


Fig. A.12 HTHFS output from run 12

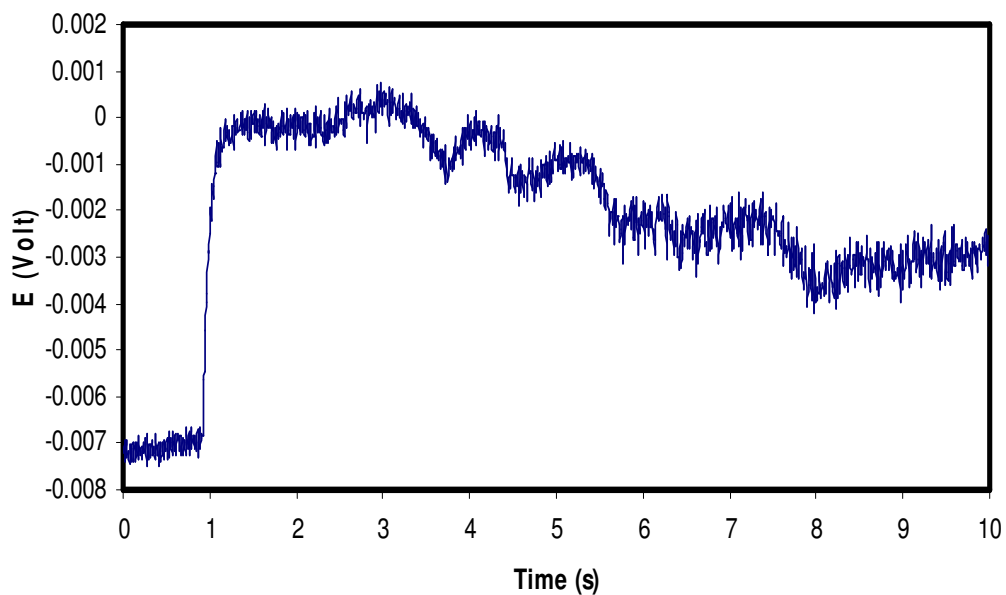


Fig. A.13 HTHFS output from run 13

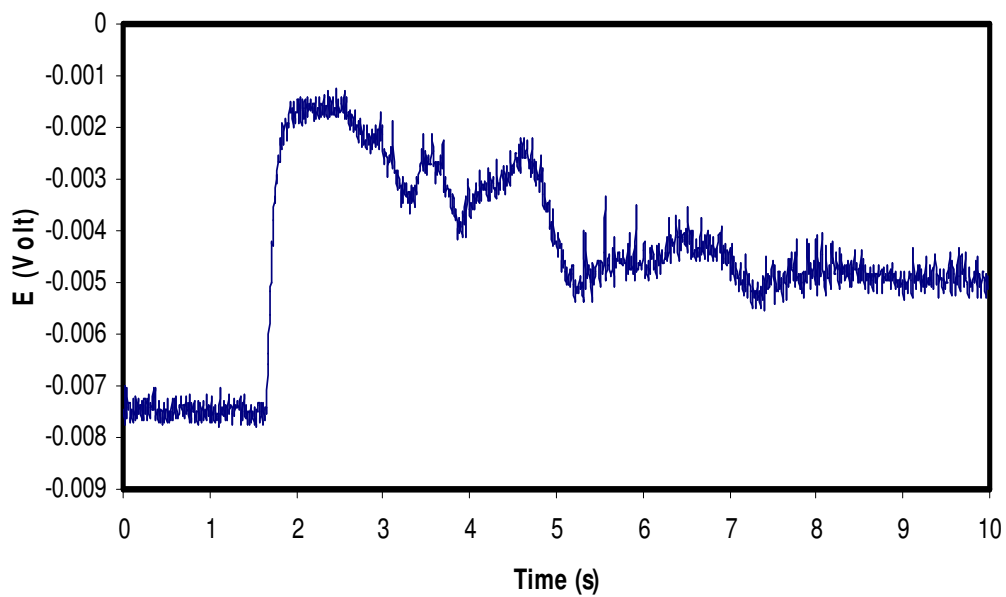


Fig. A.14 HTHFS output from run 14

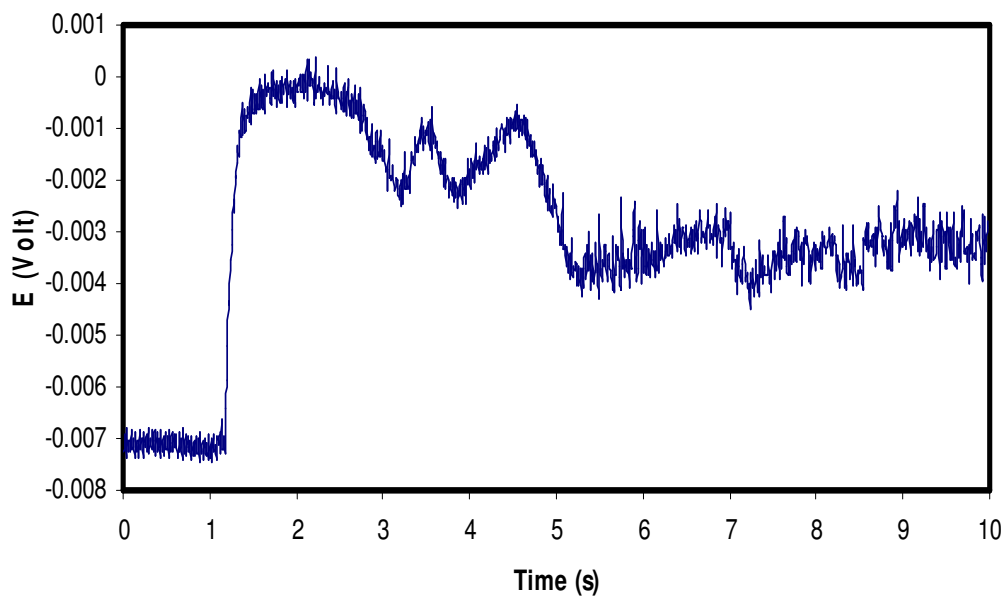


Fig. A.15 HTHFS output from run 15

Appendix B

Experimental Determination of Seebeck Coefficient of Brass and Steel Junction

Introduction

A new heat flux sensor that can function reliably in high heat flux and high temperature environments has been designed and tested. The sensor (HTHFS) was tested and calibrated using convection heat flux. The sensitivity of the HTHFS was determined from the calibration data. Theoretical value for the sensitivity was needed for verification of the results. The Seebeck coefficient of brass and steel was needed to calculate the theoretical sensitivity of the sensor. The objective of this experiment is to determine the Seebeck coefficient of brass and steel.

Apparatus and Procedure

For this experiment, a sample brass plate, a plain steel plate, a Type-T thermocouple, and a voltmeter were used. The copper wire and the constantan wire from the Type-T thermocouple were soldered to the end of the brass plate as shown in Fig. B.1. Thus a copper-brass and constantan-brass thermocouple junction was formed at either ends of the plate. A similar test setup is made with the steel plate.

The procedures for the experiment are given as follows. The brass plate is immersed in a large beaker filled with melting ice (Fig. B.2). Only one end of the plate comes into contact with the ice. The brass plate was kept in ice only long enough for the voltage measurements to be taken. This was done to avoid the entire plate from reaching the melting ice's temperature. The voltage measurements are taken between copper and brass junctions that are at room temperature and at the melting temperature of ice. Four voltage readings are taken for each data set. A set protocol was maintained to ensure that the polarities of the terminals do not get changed between different data sets. Fig. B.3 shows how the voltage was measured between the junctions.

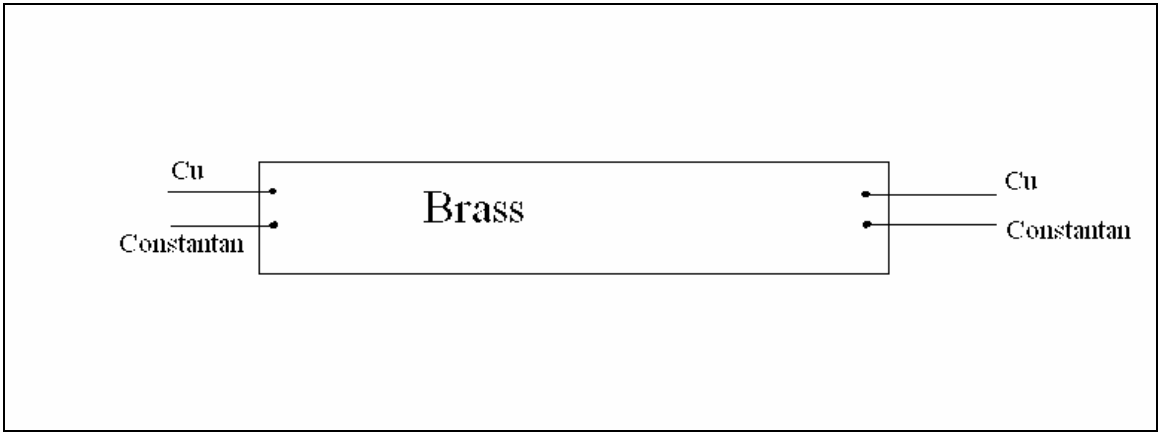


Fig. B.1 Brass plate with type-T thermocouples

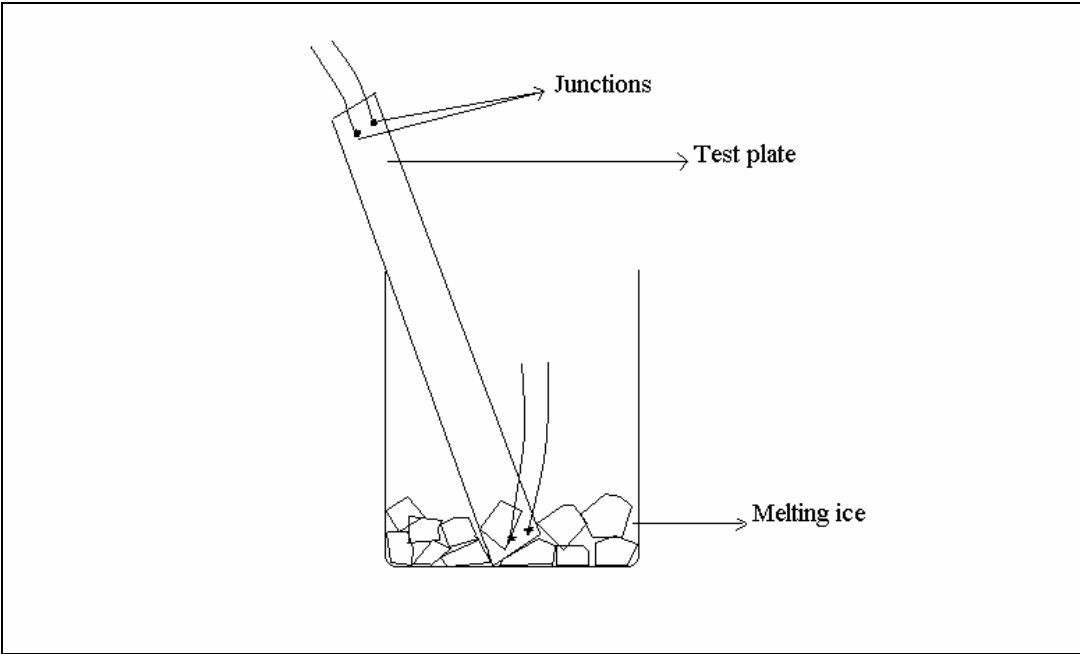


Fig. B.2 Brass plate in contact with melting ice

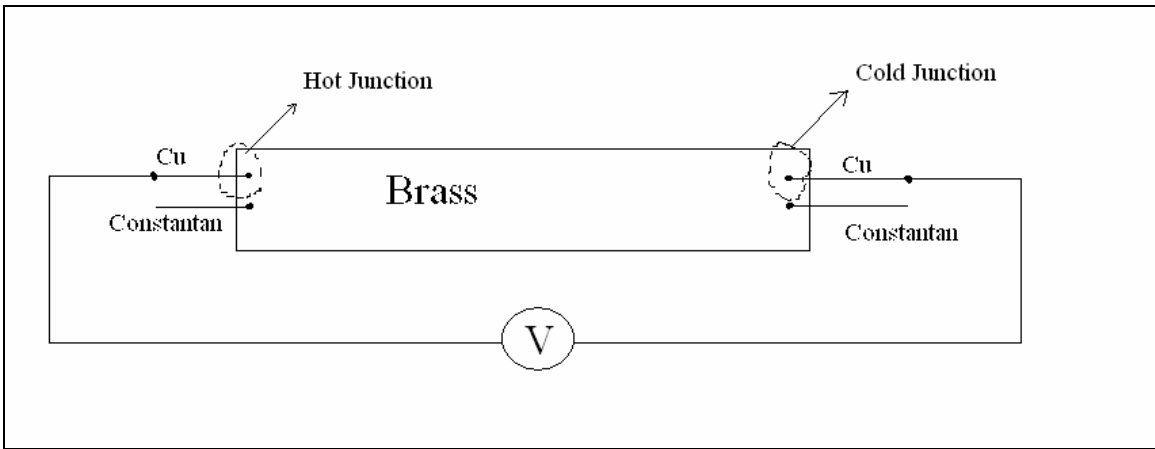


Fig. B.3 Voltage measurement between cold and hot junction

The voltage between Cu/brass junction at room temperature (from now on will be referred to as hot junction) and the Cu/brass junction at the melting ice temperature (from now on will be referred to as cold junction) was measured and recorded. The voltage outputs from the type-T thermocouple junctions at the hot junction and the cold junction were recorded. This was done to determine the temperature of the cold and the hot junction. The voltage readings for each data set were taken in rapid succession with as little time interval possible between each measurement to reduce errors due to discrepancy in the temperature that could be caused by the time lag. The above mentioned procedures were repeated with the constantan/brass, Cu/steel, and constantan/plain steel junctions and thus four data sets were obtained (Tables B.1 - B.4).

Raw Data

Table B.1 Voltage between the Cu-Brass hot and cold junction

Hot junction – Cold junction (μV)	Type-T thermocouple output at the hot junction (μV)	Type-T thermocouple output at the cold junction (μV)
+34	+30	+770
+38	+10	+820
+38	+66	+860
+35	+77	+852
+32	+59	+760
+29	+71	+754

Table B.2 Voltage between the Constantan-Brass hot and cold junction

Hot junction – Cold junction (μV)	Type-T thermocouple output at the hot junction (μV)	Type-T thermocouple output at the cold junction (μV)
-682	+121	+809
-656	+153	+828
-618	+171	+830
-625	+183	+834
-798	-60	+760
-817	-30	+789
-770	+17	+809

Table B.3 Voltage between the Cu-Steel hot and cold junction

Hot junction – Cold junction (μV)	Type-T thermocouple output at the hot junction (μV)	Type-T thermocouple output at the cold junction (μV)
-156	+228	+836
-156	+236	+845
-154	+235	+847
-153	+226	+819
-153	+237	+824
-154	+234	+812
-195	+121	+787
-161	+142	+732

Table B.4 Voltage between the Constantan-Steel hot and cold junction

Hot junction – Cold junction (μV)	Type-T thermocouple output at the hot junction (μV)	Type-T thermocouple output at the cold junction (μV)
-643	+268	+811
-674	+284	+824
-800	+110	+741
-805	+138	+771
-773	+161	+762
-685	+271	+790
-692	+292	+833

Data Analysis

The voltage outputs from the type-T thermocouples at the cold and hot junction were converted to temperature values using previously tabulated data on type-T thermocouples [16]. Difference between the two temperature values gives the actual temperature difference ΔT between the hot and the cold junctions. The sensitivity coefficient or the Seebeck coefficient of the particular metal combination was calculated by dividing the voltage output measured between the cold and hot junctions by the ΔT value. This is done for each data set and a sensitivity coefficient is determined for each data set and finally the average value is taken as the sensitivity coefficient of that particular metal combination (Tables B.5 – B.8). To obtain the Seebeck coefficient of junctions formed by brass and plain steel, the following equations were used.

$$S_{\text{brass/steel}} = S_{\text{Cu/brass}} - S_{\text{Cu/steel}} \quad (\text{B.1})$$

$$S_{\text{brass/steel}} = S_{\text{Constantan/brass}} - S_{\text{Constantan/steel}} \quad (\text{B.2})$$

In this experiment, copper and constantan have been used as the reference metals for determining the Seebeck coefficients of brass and steel combination. The reason for using both copper and constantan as the reference metal is to verify if the final Seebeck coefficient obtained using the two different reference metals match.

Results

Table B.5 Sensitivity coefficient of brass (Reference Material – Copper)

Hot junction – Cold junction (μV)	ΔT ($^{\circ}\text{C}$)	Sensitivity coefficient ($\mu\text{V}/^{\circ}\text{C}$)
+34	18.756	1.813
+38	20.5	1.854
+38	20.058	1.895
+35	19.576	1.788
+32	17.762	1.802
+29	17.304	1.676
		Average = 1.805

Table B.6 Sensitivity coefficient of brass (Reference Material – Constantan)

Hot junction – Cold junction (μV)	ΔT ($^{\circ}\text{C}$)	Sensitivity coefficient ($\mu\text{V}/^{\circ}\text{C}$)
-682	17.386	-39.227
-656	17.027	-38.527
-618	16.615	-37.195
-625	16.408	-38.091
-798	20.825	-38.319
-817	20.700	-39.469
-770	20.052	-38.4
		Average = -38.46

Table B.7 Sensitivity coefficient of steel (Reference Material – Copper)

Hot junction – Cold junction (μV)	ΔT ($^{\circ}\text{C}$)	Sensitivity coefficient ($\mu\text{V}/^{\circ}\text{C}$)
-156	15.304	-10.193
-156	15.325	-10.179
-154	15.399	-10.001
-153	14.935	-10.244
-153	14.773	-10.357
-154	14.56	-10.577
-195	16.847	-11.575
-161	14.934	-10.781
		Average = -10.49

Table B.8 Sensitivity coefficient of steel (Reference Material – Constantan)

Hot junction – Cold junction (μV)	ΔT ($^{\circ}\text{C}$)	Sensitivity coefficient ($\mu\text{V}/^{\circ}\text{C}$)
-643	13.665	-47.056
-674	13.572	-49.661
-800	15.98	-50.064
-805	16.012	-50.275
-773	15.197	-50.865
-685	13.075	-52.390
-692	13.588	-50.927
		Average = -50.18

The Seebeck coefficient of brass and plain steel junctions were calculated using equation B.3.

$$S_{\text{brass/steel}} = S_{\text{brass}} - S_{\text{steel}} \quad (\text{B.3})$$

Two values for the Seebeck coefficient of the brass-steel combination was calculated, one from the data using copper as reference material and the other from the data using constantan as reference material. The two values were $12.3 \mu\text{V}/^\circ\text{C}$ and $11.72 \mu\text{V}/^\circ\text{C}$. The percent difference between the two values was computed to be 4.72%. So, the difference between the two values is not statistically significant. So, the average of the two values was taken as the final value for the Seebeck coefficient of the brass/steel combination. The Seebeck coefficient of a brass and steel junction was determined to be $12.01 \mu\text{V}/^\circ\text{C}$.

Appendix C

Calibration of a SB Heat Flux Gage

by

Sujay Raphael-Mabel and Tom Diller
Virginia Tech

Introduction

Schmidt-Boelter heat flux gages are used to measure heat flux going into or out of a surface due to convective heat transfer. The present experiment was conducted to calibrate a Schmidt-Boelter (SB) heat flux gage in convection using the substitution method with an HFM. The results as a function of heat transfer coefficient were compared with the manufacturer's radiation calibration. The method used in the experiment was heat transfer by air-jet impingement normal to the surface of the heat flux gage.

Apparatus

The Schmidt-Boelter heat flux gage that was tested was manufactured by MedTherm Corporation. The signal was amplified using a 100 gain amplifier designed and built by Jonathon McGlumphy, a graduate student at Virginia Tech. The air supply for the air jet was provided by a large pressure vessel pressurized to about 120 psi using an external compressor. The strength of the air flow was controlled by a valve. The data acquisition equipment used in this experiment was a 64 channel junction box that had a built in A/D converter connected to a computer. The data was acquired and visualized using Lab VIEW with a sampling rate of 20 Hz for 30 second duration.

An existing piece of test equipment was used consisting of an aluminum plate, an aluminum nozzle holder and two aluminum channels. The aluminum plate was machined to the following dimensions: 10" x 6" x 5/8". Three circular holes with diameters 1.5",

1/4", and 1/16" were drilled in the plate. The positions of the holes on the plate are shown in Fig. C.1.

The two aluminum channels had a length of 18 inches and a width and height of 7/8". Three plates of aluminum were welded together to hold the nozzle for the air jet. The dimensions of the holder are 7.25" x 4.25" x 2". The two channels are welded to the legs of the aluminum nozzle holder (Fig. C.2) such that the distance between the two channels is 6.25 inches. The complete test setup is shown in Fig. C.3.

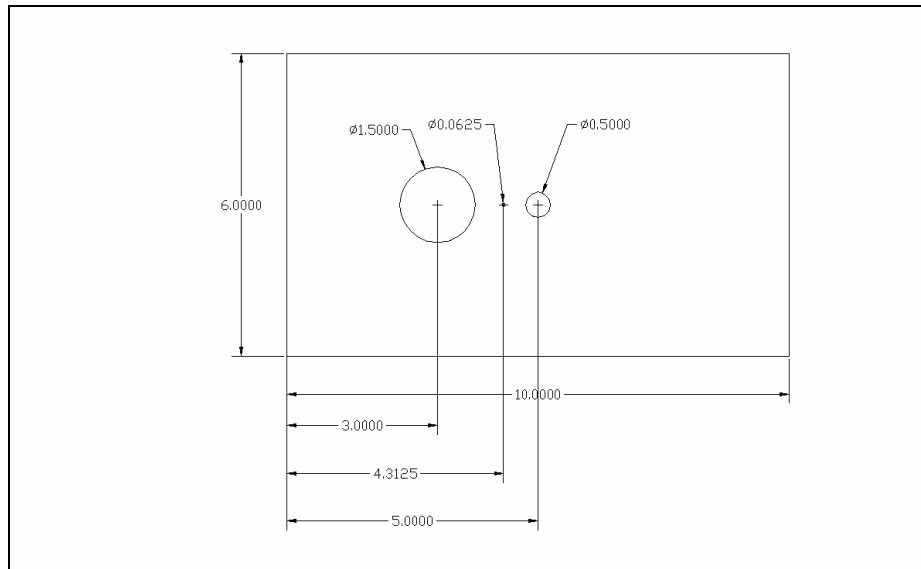


Fig. C.1 Top view of test plate

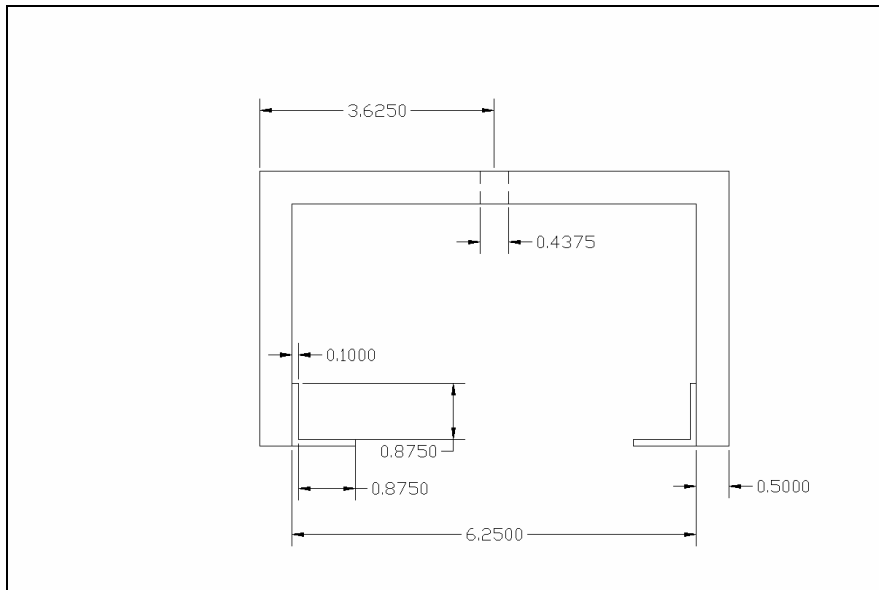


Fig. C.2 End view of channel and nozzle holder

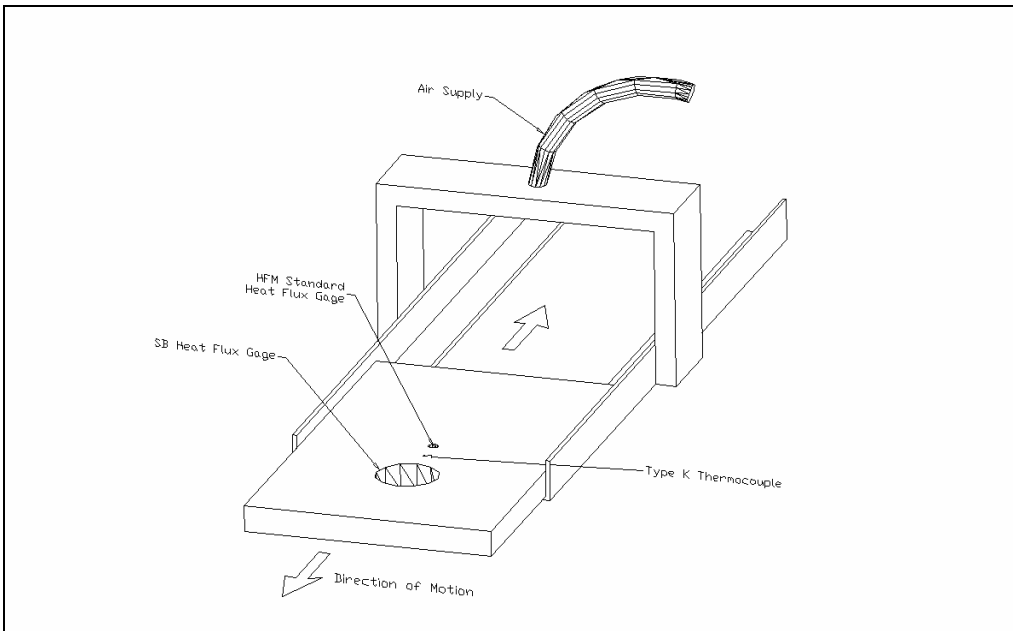


Fig. C.3 Assembled test equipment

Procedure

The SB heat flux gage, the type K thermocouple and the HFM standard heat flux gage were inserted into the holes drilled for them in the aluminum plate. The thermocouple was soldered into a 1/16" O.D. copper tube, which was then press fit into the plate. The outputs from the SB heat flux gage and the HFM standard heat flux gage were connected to the amplifier, whose output signals were sent to the junction box. The amplifiers were zeroed out using a voltmeter. The tube carrying the airflow was connected to a coil shaped copper pipe immersed in either boiling water or ice water to provide the temperature difference between the flow and the plate. A type-K thermocouple was inserted into the tube connecting the pressure vessel and the air-jet nozzle such that it measures the total temperature of the airflow after the air flows through the heated region. The signals from the thermocouples placed in the air flow and in the plate were fed into the junction box.

The test setup was placed on two wooden supports. The aluminum plate with the heat flux gages and a thermocouple connected to it was placed under the aluminum nozzle holder such that it slides along the aluminum channels. Three sets of zero input data from the heat flux gages were acquired. Then the heated air jet was impinged upon the plate and the plate is moved manually along the channels slowly such that the air jet impinges directly on the SB heat flux gage and the HFM heat flux gage at least once during the 30 seconds of data acquisition time. This step was repeated for increasing strength of the air jet and the corresponding data was acquired for each run. The data sets consist of the time, the voltage signals from the SB, HFM heat flux gages, and temperature readings from the thermocouples inserted into the air flow and the plate.

Data Reduction

Microsoft Excel was used to reduce and analyze the data. The data was imported into MS Excel and stored as excel files. The values of the heat transfer coefficients in the flow were obtained from the voltage signal from the HFM using equation C.1. The average zeroes for each data channel were used to adjust the measured values.

$$h = \frac{(\text{Output Signal} - \text{Average Zero Error})}{(\text{Air Temp} - \text{Plate Temp}) \times (\text{Amplifier Gain}) \times (\text{HFM Sensitivity})} \left(\frac{W}{cm^2 \cdot ^\circ C} \right) \quad (C.1)$$

Two different HFM gages were used during the experiment with sensitivities of $142.9 \mu V/(W/cm^2)$ and $100 \mu V/(W/cm^2)$. Using this equation, the heat transfer coefficients sensed by the HFM gage throughout the run were obtained, as illustrated in Fig. C.4. The peak heat transfer coefficient was used to characterize the condition directly under the jet. To reduce the errors caused by noise, the peak value was calculated using about ten points around the peak. Based on these results the sensitivity of the SB heat flux gage was computed using equation C.2.

$$S = \frac{(\text{Output Signal} - \text{Average Zero Error})}{(\text{Air Temp} - \text{Plate Temp}) \times (\text{Amplifier Gain}) \times (\text{Peak } h)} \left(\frac{mV}{kW / m^2} \right) \quad (C.2)$$

The values from equation C.2 were computed throughout the test time, as illustrated in Fig. C.5. The peak value was taken as the actual sensitivity of the SB heat flux gage, corresponding to the time when the jet was directly over the gage. Again, to reduce the effects of noise, the average of eight values to ten values around the peak was used. The corresponding temperatures for the test are shown in Fig. C.6. The typical driving temperature difference was $30^\circ C$.

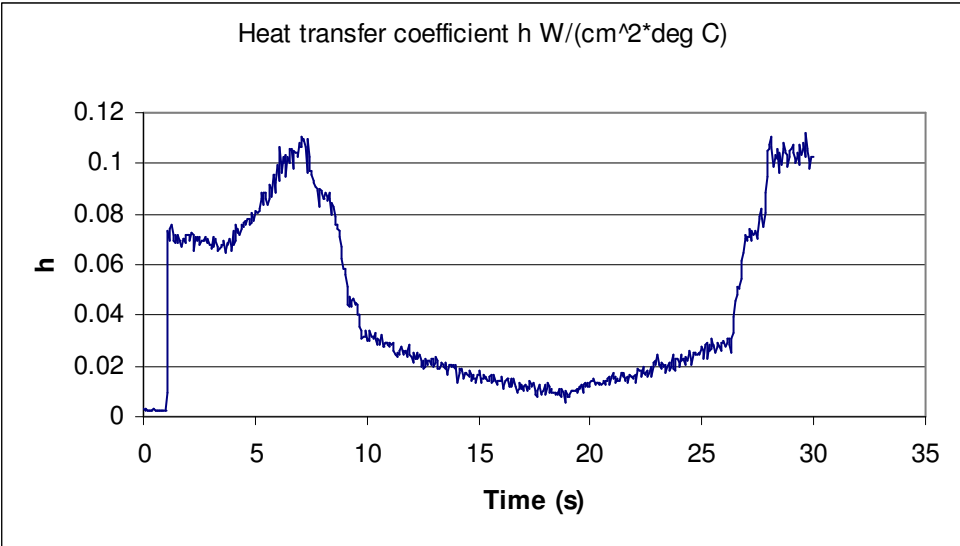


Fig. C.4 Sample heat transfer coefficient trace

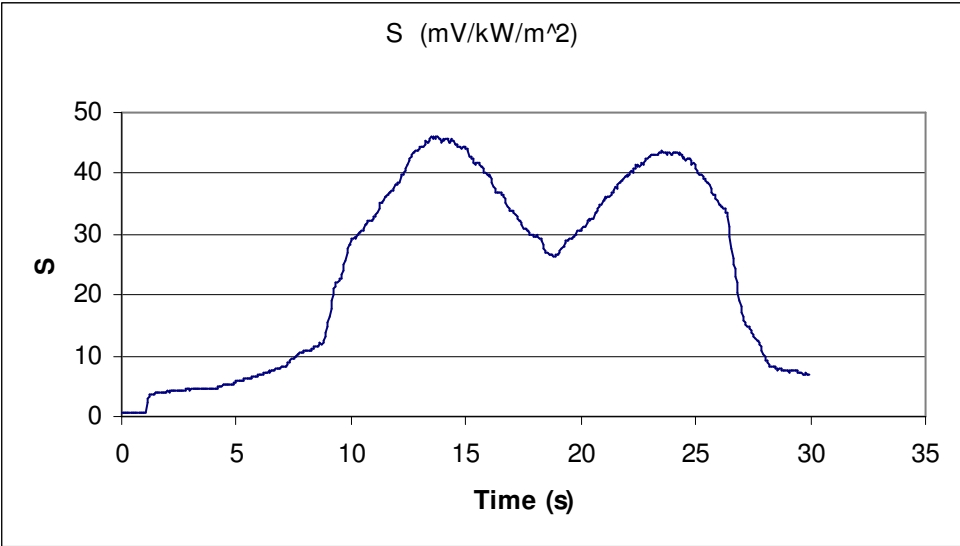


Fig. C.5 Schmidt-Boelter sensitivity calculation

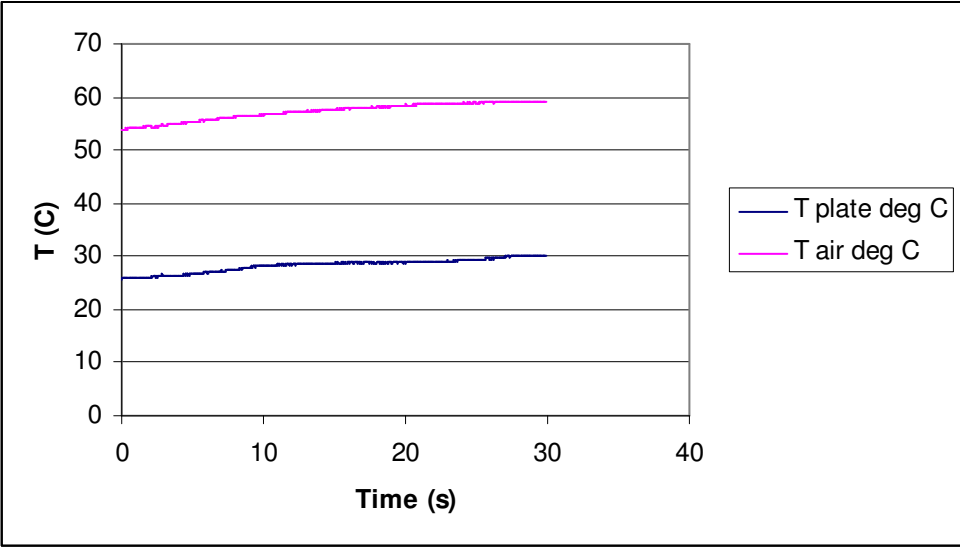


Fig. C.6 Air and plate temperatures

Results

The computed values of the heat transfer coefficients and the corresponding SB heat flux gage sensitivity values are listed chronologically in the table. A rigorous uncertainty analysis has not been performed on these experiments. Based on previous experience the absolute uncertainty is estimated as $\pm 20\%$ and the relative uncertainty between tests as $\pm 10\%$. The major contributors are the HFM sensitivity (calibration), the measurement of the heat transfer coefficient and assumption of a constant value, and the measurement and interpretation of the air and plate temperatures. It's estimated that the uncertainties could be halved if a facility was built specifically for this testing with two jets for simultaneous measurement with both gages. It would also be helpful to have a separate measurement of the temperature of the copper body of the Schmidt-Boelter gages.

Table C.1 Results from the calibration test

Test Run	h (W/m ² -K)	S (mV/kW/m ²)
24/02	1271	40.3
24/03	1047	45.8
24/04	1028	47.8
25/01	1089	47.6
25/02	363	53.2
25/03	338	55.5
25/04	456	50
25/05	437	51.75
25/06	206	54
25/07	199	54.7
25/08	1120	47.1
25/09	1635	45.8
25/11	349	49.8
25/12	228	53.5
26/01	245	66.1
26/02	325	57.6
26/03	370	56.4
26/05	443	60
26/06	588	54.7
26/07	462	52.9

Vita

Sujay Raphael-Mabel was born in Chennai, India in a government hospital on June 80, 1980. He lived with his family in Chennai where he did all his schooling. Growing up near an airport, the author has a great interest in airplanes and aviation. At the age of 18, he moved to Arizona to begin his undergraduate education in aerospace engineering at Embry-Riddle Aeronautical University. He received his Bachelor of Science in Aerospace Engineering in the Spring of 2002, graduating Magna Cum Laude. He went back to India for a little more than a year and taught Physics to high school students. In the Fall of 2003, he began his graduate studies at the Virginia Polytechnic Institute and State University in Blacksburg, VA working as a graduate assistant for Dr. T.E. Diller studying heat transfer and conducting research on heat flux sensors. The author defended his work on February 16, 2005, and will be working for Merlin Simulations, Inc. in Dulles, VA as a Systems Analyst.

Sujay A. Raphael-Mabel